Nanoscale
Advances

ROYAL SOCIETY
OF CHEMISTRY

REVIEW

View Article Online
View Journal | View Issue

Check for updates

Cite this: *Nanoscale Adv.*, 2021, **3**, 41

Sonochemical catalysis as a unique strategy for the fabrication of nano-/micro-structured inorganics†

Zhanfeng Li,[a] Jun Dong,[a] Huixin Zhang,[a] Yongqiang Zhang,[c] Huiqi Wang,[a] Xuejun Cui[b] and Zonghua Wang*[a]

Received 8th September 2020
Accepted 22nd October 2020

DOI: 10.1039/d0na00753f

rsc.li/nanoscale-advances

Ultrasound-assisted approaches, as an important trend in material synthesis, have emerged for designing and creating nano-/micro-structures. This review simply presents the basic principles of ultrasound irradiation including acoustic cavitation, sonochemical effects, physical and/or mechanical effects, and on the basis of the latest progress, it newly summarizes sonochemical catalysis for the fabrication of nano-structured or micro-structured inorganic materials such as metals, alloys, metal compounds, non-metal materials, and inorganic composites, where the theories or mechanisms of catalytic synthetic routes, and the morphologies, structures, sizes, properties and applications of products are described in detail. In the review, a few technological potentials and probable challenges of sonochemical catalysis are also highlighted for the future advance of synthesis methods. Therefore, sonochemical catalysis or ultrasound-assisted synthesis will serve as a unique strategy to reveal its great significance in material fabrication.

1. Introduction

Sonochemistry, coined in 1953, is a research area in which powerful ultrasound irradiation can assist to induce some chemical reactions (synthesis, degradation, catalysis, *etc.*),[1] or it is defined as a nonclassical mechanical method by which one or more chemical processes can be induced or strengthened or even weakened when a reacting system is irradiated with ultrasound. Since sonochemistry or the chemical effects from ultrasound irradiation were reported firstly in the 1920s or earlier, many important sonochemistry-based applications have been found in chemical synthesis, material processing, industrial manufacturing, and so on.[2] For instance, ultrasound irradiation is a very efficient method to clean the debris from solid surfaces, which has been widely used in research and industry;[3] ultrasound irradiation is often utilized to purify wastewater by

Dr Zhanfeng Li is an associate professor at the College of Chemistry and Chemical Engineering of Qingdao University. He received his PhD degree in applied chemistry from Jilin University in 2016, under the supervision of Prof. Xuejun Cui. After joining Qingdao University, he worked as a Postdoctoral Research Fellow at the College of Materials Science and Engineering (Qingdao University), under the supervision of Prof. Zonghua Wang. His research interests focus on sonochemical synthesis, the design of new micro-/nano-scale materials, and sonochemical applications in catalysis and biomedicine.

Dr Huiqi Wang is a lecturer at the College of Chemistry and Chemical Engineering of Qingdao University. She received her PhD degree in analytical chemistry from Jilin University in 2018, under the supervision of Prof. Qiong Jia. After graduation, she joined Qingdao University and worked as a Postdoctoral Research Fellow at the College of Materials Science and Engineering (Qingdao University), under the supervision of Prof. Zonghua Wang. Her research interests focus on the design of new nano-materials, fabrication of functional adsorbing materials, and applications in biological detection and analysis.

---

[a] *Shandong Sino-Japanese Center for Collaborative Research of Carbon Nanomaterials, Instrumental Analysis Center, College of Chemistry and Chemical Engineering, Qingdao University, 266071 Qingdao, China. E-mail: wangzonghua@qdu.edu.cn*

[b] *College of Chemistry, Jilin University, 130012 Changchun, China*

[c] *Junan Sub-Bureau of Linyi Ecological Environmental Bureau, 276600 Linyi, China*

† Electronic supplementary information (ESI) available. See DOI: 10.1039/d0na00753f

degrading contaminants (*e.g.*, textile dyes);[4,5] and in polymer chemistry, ultrasound irradiation can be used as a driving force to cleave polymer chains,[6,7] or act as a simple but effective way to initiate radical-mediated polymerizations or to carry out emulsion polymerizations by emulsifying oil and water phases.[8–10]

Nano-structured or micro-structured materials are interesting and versatile in many applications such as catalysis, biomedicine, energy storage, hydrogen storage, *etc.*,[11–13] so numerous synthesis methods have been developed to prepare well-designed functional materials, where sonochemistry serving as a unique catalytic technology is often involved. This review will overview the latest developments of ultrasound-assisted effects or reactions to prepare nano-scale and micro-scale inorganic structures, give a fundamental understanding of the basic principles of sonochemistry, and cover the powerful and unique aspects in the synthesis of products (*i.e.*, metals, alloys, metal compounds, and non-metal materials) as a greater emphasis, *e.g.*, the morphologies, structures, sizes, properties as well as applications. As well, the fabrication of multimodal or multifunctional inorganic composites (*e.g.*, metal/metal compounds, metal/non-metal materials, metal compound/metal compound, metal compound/non-metal material) will be a focus. Meanwhile, the review will point out the prospective challenges and trends in the programming of ultrasound-assisted preparation, and conclude with the significance of sonochemical catalysis in material synthesis.

2. Ultrasound

Ultrasound refers to a concept or terminology in which a sound wave has a frequency higher than 20.0 kHz exceeding the upper limit of human hearing, and its industrial production can be often achieved by the electrical energy from a magneto-strictive or piezo-electric transducer.[14–16] A piezo-electric transducer is able to create ultrasound irradiation across the whole frequency range, but the element is more fragile and destroyed by heat. In comparison, the ultrasonic frequency produced by a magnetostrictive transducer, for practical reasons, is restricted to be 20.0–100.0 kHz.[17] For ultrasound, the frequency that is governed by the transducer is a key factor for many applications. Low-frequency ultrasound (20.0–100.0 kHz) is usually called power ultrasound, and the majority of sonochemical processes as well as ultrasound-assisted surface treatments occurs in this frequency range.[3,18] For example, cleaning or decontamination is the most common use of low-frequency ultrasound in a general chemistry laboratory. High-frequency ultrasound (0.5–10.0 MHz) is typically used in medical applications for diagnosis and therapy.[19–21] For example, high-intensity focused ultrasound (HIFU) can be used in surgery to break down blood clots or destroy tumors, and the ultrasound irradiation at a frequency of around 1.0 MHz has aided the delivery of some nanodrugs. Fig. 1 shows the general applications of ultrasound, and many of them are briefly explained in terms of chemical technology.

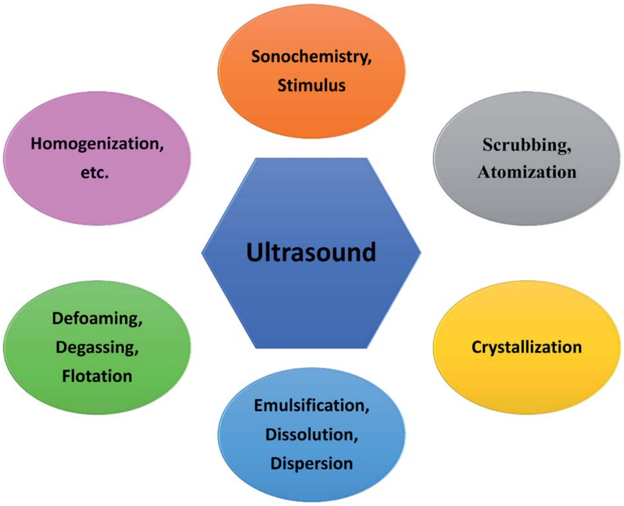

Fig. 1 General applications of ultrasound in chemical, material and manufacturing processes.

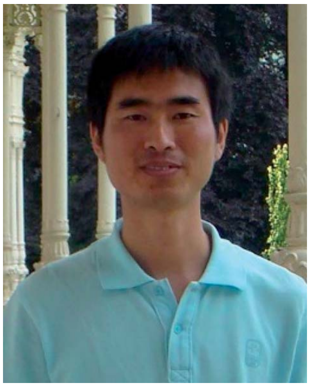

Dr Xuejun Cui is a professor in the Department of Chemistry at the University of Jilin. He graduated in applied chemistry in 2003 and completed his PhD at Jilin University in 2008, under the supervision of Prof. Hongyan Wang. After that, he joined the faculty of the Chemistry Department in Jilin University. During the employment, he spent time as a junior research fellow at the Max Planck Institute of Colloids and Interfaces and Nanyang Technological University. His research interests focus on acoustic chemistry, and the design and preparation of biomedical materials for drug delivery.

Prof. Zonghua Wang is a Group Leader at the Department of Chemistry, and a Director of Instrumental Analysis Center, Qingdao University. She obtained her M.S. degree in analytical chemistry from China University of Geosciences in 1987, and obtained her PhD in analytical chemistry from Tsinghua University in 2004, under the supervision of Prof. Guoan Luo. Her current research interests include the functionalization and application of nanomaterials, nano-analytical chemistry, electroanalytical chemistry, and biofunctional interfaces and materials.

2.1. Acoustic cavitation

When sound spreads in a liquid, its typical velocity and wavelength are both much larger than the molecular scale, so theoretically no direct interaction can occur at a molecular level between ultrasound irradiation and chemical species.[22,23] However, ultrasonic irradiation, different from heat, light or other energy sources, can offer some extreme transient conditions (*e.g.*, localized high pressure and temperature) and physical and/or mechanical effects to complete some chemistry-correlative applications, and the whole processes are basically induced by acoustic cavitation created from either low-frequency or high-frequency ultrasound.[24]

Acoustic cavitation is an instantaneous process spanning the formation, growth and violent collapse of micro-sized bubbles which are caused by ultrasound irradiating a liquid.[25] As we know, ultrasound is a longitudinal pressure wave, and when the sound moves and propagates through a medium, the acoustic pressure cycles will cause the medium containing gas or particles to experience an alternate compression and rarefaction phase. The cavitation bubbles are usually nucleated during the rarefaction phase, because some liquid molecules may be pulled apart at "weak spot" sites containing some gaseous impurity by overcoming intermolecular interactions.[26] Following this, the bubbles will grow in every acoustic pressure cycle along with a gas inflow, where the average bubble size during the rarefaction phase is larger than that during the compression phase. During the oscillating process, the bubbles accumulate ultrasonic energy effectively causing an enormous energy concentration within their small volume. The bubbles will be no longer stable after growing to a critical size range of typically tens of micrometers, and they go through a rapid inertial overgrowth by strongly coupling to the acoustic field until a catastrophic collapse occurs at some point. Once collapsing, the concentrated energy stored in the bubbles will be released within a very short time at a heating and cooling rate higher than a billion K s^{-1}, and moreover, such implosive collapse is a nearly adiabatic process, resulting in the formation of localized micro-scale "hotspots" with high temperature (≈ 5000 K) and high pressure (≈ 1000 bar).[27,28] Fig. 2 shows the formation of a "hotspot" under acoustic cavitation.

2.2. Sonochemical effects

Since acoustic cavitation is able to account for the extreme characteristic conditions to induce some possible chemistry effects, the hotspot theory has been postulated to explain sonochemical events, though many phenomena reported by several researchers still contradict it.[2] In a liquid system, there is no direct chemical reaction except the sonolysis of liquid, but the sonolysis-inducing radicals may diffuse into the liquid to create potential chemical reactions, which involve primary or secondary sonochemical reactions (Fig. 2). Once the cavitation bubbles collapse, the conditions in the bubble center or at the hotspots are very harsh, *e.g.*, large temperature gradients, pressure and shear are experienced. The volatiles and/or gases inside the bubbles (Zone 1) and/or in the interfacial region (Zone 2) between the bubble center (Zone 1) and the bulk liquid (Zone 3) will lead to the formation of many radical species, namely primary sonochemical reactions. The majority of radical production is thought to occur in the interior vapor phase of bubbles, because the liquid layer surrounding the cavitation bubbles will immediately inject into the bubbles upon cavitation collapse. When the initially produced species migrate into the surrounding liquid, a variety of reactions with solutes may create secondary sonochemical reactions.[29] What is more, the sonochemical effects involve different types of cavitation bubbles. In the system, the transient bubbles, which often grow and collapse quickly after one acoustic cycle, may account for the majority of chemical activity. Differently, the stable bubbles which can persist for more acoustic cycles will create a large shear gradient when collapsing, and the shear gradient plays an important role in the sonochemical system. For example, ultrasound irradiation is able to contribute to the efficient formation of emulsions in a two-phase liquid system.[30]

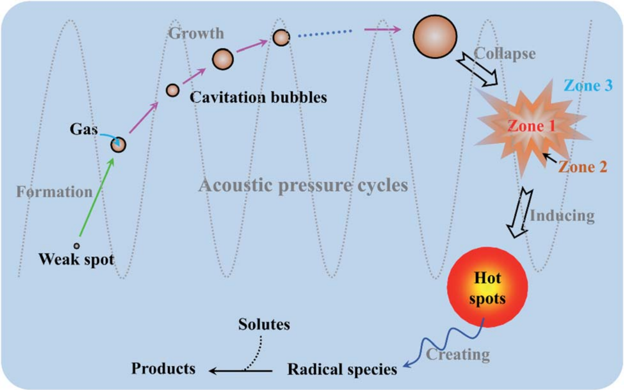

Fig. 2 Schematic illustration of "hotspot" formation under acoustic cavitation, and the reaction zones of sonochemistry.

Like other chemical reactions or processes, sonochemistry also involves the dissociation and formation of chemical bonds, since the compressive heat created by collapsing bubbles generates high enough temperatures locally. In order to confirm this proposal, Pflieger *et al.* carried out the sonolysis of water at different ultrasound frequencies and photographically captured the generated highly reactive hydroxyl radicals ($^{\bullet}OH$) (reaction (1)), and the addition of luminol could highlight the phenomenon owing to the blue sonochemiluminescence generated near the cavitation bubbles (Fig. S1†).[31] Upon diffusing out, the primary $H^{\bullet}$ and $^{\bullet}OH$, if taking no account of the recombination to their original form (reaction (2)), can further combine to produce H_2 and/or H_2O_2 (reactions (3) and (4)), and can also generate some secondary radicals, *e.g.*, $R^{\bullet}$ by reacting with organic additives (reaction (5)), or $HO_2^{\bullet}$ by a combination of $H^{\bullet}$ with dissolved oxygen (O_2) (reaction (6)). Either strong oxidants or reductants are capable of initiating various sonochemical reactions in aqueous or nonaqueous solution including reduction, oxidation, hydroxylation, degradation, polymerization, *etc.*

$$\mathrm{H_2O} \rightarrow \mathrm{H}^{\bullet} + {}^{\bullet}\mathrm{OH} \tag{1}$$

$$\mathrm{H}^{\bullet} + {}^{\bullet}\mathrm{OH} \rightarrow \mathrm{H_2O} \tag{2}$$

$$2H^{\bullet} \rightarrow H_2 \tag{3}$$

$$2{}^{\bullet}OH \rightarrow H_2O_2 \tag{4}$$

$$RH + {}^{\bullet}OH \text{ (or } H^{\bullet}) \rightarrow R^{\bullet} + H_2O \text{ (or } H_2) \tag{5}$$

$$H^{\bullet} + O_2 \rightarrow HO_2^{\bullet} \tag{6}$$

2.3. Physical and/or mechanical effects

Accompanied by the sonochemical consequences, the acoustic cavitation in a liquid often gives rise to numerous physical and/or mechanical effects including simple heating, shock waves and microjets (Fig. 3), which can also affect the efficiency of sonochemical reactions.[32] Heating during sonication is readily understood because tens or more of watts of acoustic energy will be delivered into the liquid, so ultrasound can be useful for activating reactions. A microjet in a liquid is often created in any heterogeneous system, since the asymmetrical collapse of highly energetic bubbles usually induces the surroundings to form a doughnut-like shape.[29] Experimentally, the microjets have high speeds, and those greater than 100 m s^{-1} can cause surface modification (pitting and erosion) or the generation of nanostructures.[33] If a surface-unperturbed bubble rebounds rapidly from its minimum spherical radius causing the surrounding liquid to compress and then to propagate outward, a shock wave will occur.[34,35] Likewise, the shock waves can produce several different mechanical and physical consequences, such as increasing the mass transport, accelerating the suspension of solid particles, and inducing changes in size distributions, morphologies and surface compositions. All in all, many ultrasound-assisted processes or technologies, *e.g.*, the fragmentation for brittle materials, the emulsification for immiscible liquids, the agglomeration for malleable materials, and the exfoliation of layered materials into 2D layers, can be explained by these physical and/or mechanical effects.[36,37]

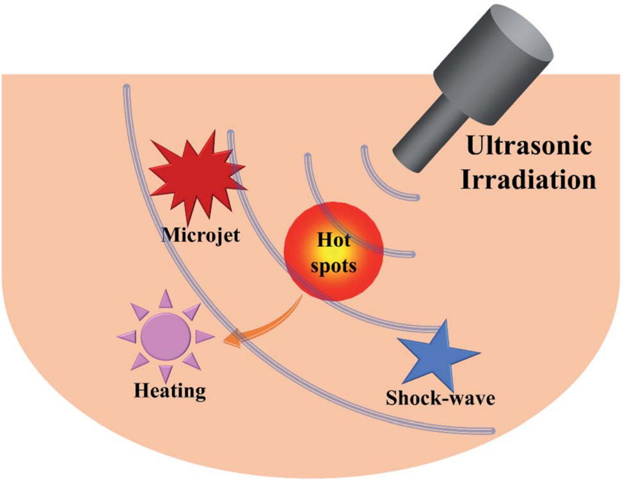

Fig. 3 Physical and/or mechanical effects from acoustic cavitation in a liquid.

3. Sonochemical catalysis to synthesize nano-/micro-structures

Nano-structured and micro-structured materials have been opening up new opportunities for many applications in electronics, catalysis, energy, chemistry, medicine and biology, because nano-/micro-sized regimes often exhibit a lot of properties distinct from those of their bulk counterparts. With a rapid advance of nanoscience and nanotechnology, a variety of synthetic methods (*e.g.*, gas phase techniques, liquid phase methods, and mixed phase approaches) have been developed to design and prepare nano-/micro-structures. Sometimes, many chemical, physical and/or mechanical properties which often prescribe the applications of nano-/micro-structured devices are heavily dependent upon the synthetic routes of materials, so that an appropriate technology will be a driving force for the new synthesis methodologies.[38,39] Among versatile methods, the utilization of ultrasound has been extensively examined for material synthesis over the years, and it is demonstrating its powerful and unique aspects in the fabrication of nano- and micro-structured materials including inorganics, polymers, and hybrid materials (Fig. 4). The specialty that ultrasound irradiation provides a facile and fast route to yield a variety of nano-/micro-materials from inorganic or organic precursors is mainly dependent on the primary and/or secondary sonochemistry, or more specifically, is decided by primary and/or secondary radicals from bubble collapse and post-produced chemical consequences in the liquid phase. In addition, physical/mechanical effects also play an important role in such formation. As an indispensable emphasis, the common types of nano/micro inorganic materials will be methodically presented in the following sections.

4. Metals and alloys

Metal nanomaterials have a useful superiority in many fields such as catalysis, sensing, imaging, biomedicine, and so on. Under

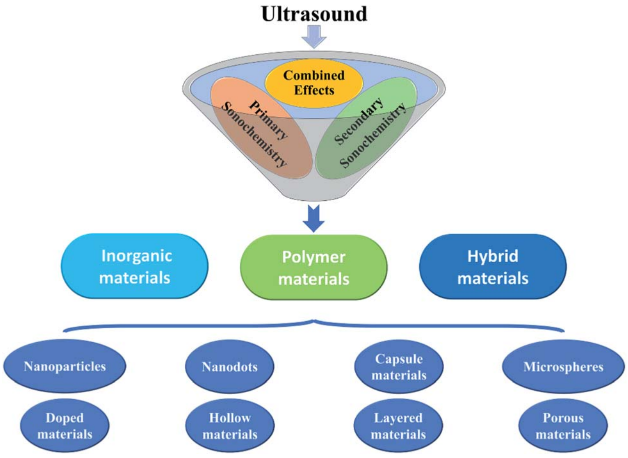

Fig. 4 Nano-/micro-structured inorganic, polymeric, and hybrid materials produced by sonochemical catalysis.

ultrasound irradiation, volatile organometallic compounds such as $Fe(CO)_5$, $Cr(CO)_6$, $Ni(CO)_4$ and $Co(CO)_3NO$ easily release individual metal atoms by dissociation of the organic groups as well as the multiple metal–ligand bonds, forming metal nanostructures in a nonvolatile solvent (*e.g.*, silicone oil, long-chain hydrocarbons). In the synthesis, the atoms of organometallic compounds can be thermally excited to the point of emitting visible light analogous to the emission from flame excitation, and the nonvolatile solvents are very significant for absorbing the available energy in the collapsing bubble, so that the achieved conditions are much less extreme.

Suslick *et al.* carried out the sonication of $Fe(CO)_5$ in alkane solvent or ionic liquid with a low vapor pressure under argon gas, which efficiently yielded a black iron powder at the freezing point.[40,41] Ultrasound irradiation generated a very high temperature within the short lifetime of a cavitation event, enabling a rapid quenching process to rapidly cool the metal atoms and prevent crystallization, so the obtained iron powder appeared to be an agglomeration of 20 nm amorphous nanoparticles. Later on, Enomoto *et al.* examined sonochemically derived amorphous metallic iron from $Fe(CO)_5$, and found that there was a certain amount (about 15%) of volatile component. By heating in an inert atmosphere, the volatile component could be removed, but the as-synthesized fine iron, if exposed to air, would be oxidized showing a weight gain. The agglomerated appearance of products would not be favorable especially for catalytic application, so oleic acid or other similar surfactants often could be present in the solvent to stabilize the metal atoms (Fig. S2-I†).[42] Interestingly, it was concluded that the surfactant addition should be done after the sonochemical synthesis rather than before the synthesis. This might be because the unfavorable sonochemical interaction between the surfactant and the carbonyl would result in large-sized product. When oleic acid (1 mass% in decane) was added after the synthesis, a fine dispersion of iron nanoparticles could be easily achieved (Fig. S2-II†).[42] Other precursor compounds also have produced porous amorphous metal nanoparticles, even alloy nanoparticles by varying the composition in the solution.[43,44]

Besides volatile organometallic compounds, a few nonvolatile precursors also can create nanostructured metals when subjected to ultrasound irradiation in a volatile solvent. Different from the metal synthesis from volatile organometallic compounds, the process of nonvolatile precursors forming metal nanostructures is mainly based on the mechanism of secondary sonochemistry, because the sonolysis of solvent vapor can produce some strong debris but does not need additional catalysts,[45] for example, $H^•$ and $^•OH$ radicals for water, $R^•$ radicals for volatile organic vapor, and so on. The reactive debris are responsible for producing nano-/micro-structured materials *via* some redox reactions. Moreover, the products from nonvolatile compounds are usually well crystallized, which is obviously different from the amorphous structures created by volatile precursors.

As a useful alternative to the traditional approaches (*e.g.*, photochemical reduction, controlled chemical reduction, radiolytic reduction, and solvothermal synthesis), the sonochemical preparation of nanostructured noble metals (*e.g.*, Au, Ag, Pt, Pd, *etc.*) has been carried out in many studies. Grieser and coworkers published a systematic study on the sonochemical synthesis of gold nanospheres.[46] When $HAuCl_4$ was sonicated in aqueous solution containing alcohols or other similar organic additives, spherical gold nanoparticles would be formed by Au(III) reduced to Au(0), and the nanoparticle size was related to the ultrasound frequency. At around 213 kHz in the presence of 1-propanol, the size of gold nanoparticles was smallest owing to the maximum rate of Au(III) reduction (Fig. 5-I). Yasuda *et al.* synthesized size-controlled gold nanoparticles by using the ultrasound irradiation of $HAuCl_4$ aqueous solutions with the aid of ultrafine bubbles (UFBs) rather than any capping and reducing agents.[47] The addition of air-UFBs largely decreased the diameter of the spherical gold nanoparticles, which was attributed to the sonochemical reduction of Au(III) ions being accelerated by the air-UFBs. And because gold nanospheres electrostatically adsorbed onto those UFBs with a long lifetime in water, the product was very stably dispersed in an aqueous solution for more than two months (Fig. 5-II). Additionally, pulsed ultrasound delivered with the same time-averaged power as continuous irradiation could further decrease the nanoparticle diameter.

Nonspherical metal nanoparticles such as nanorods, nanobelts, nanocones, nanoplates, nanowires, and nanorings can also be prepared by sonochemical reduction. For example, Au nanorods have been formed from $HAuCl_4$ in the presence of cetyltrimethylammonium bromide and $AgNO_3$,[48] when the formation of monodispersed Au nano-decahedra was realized with poly(vinylpyrrolidone) as a stabilizing polymer.[49] Ashokkumar *et al.* reported the sonochemical synthesis of different gold nanoparticles by using HIFU at 463 kHz, and the shapes and size distributions of products were dependent on the ultrasound condition.[50] In this case, the radical-driven reduction process played an important role in nuclei formation and growth, and thus the size of gold nanoparticles decreased with acoustic power increasing. Experimentally, irregular shapes appeared at 30 W, and primarily icosahedral occurred at 50 W with a significant amount of nanorods at 70 W. Significantly, some nonvolatile precursors under high-intensity ultrasound irradiation were capable of creating extremely small nanoclusters (*e.g.*, Ag nanoclusters, Au nanoclusters and Cu nanoclusters) when using polymer molecules as a capping agent.[51–55] To avoid the resource-/time-consuming synthesis processes of nanoclusters, Xin *et al.* utilized a rapid sonochemical route to prepare fluorescent Au nanoclusters (about 2 nm) in a large quantity within about 40 min (Fig. S3-I†).[56] The Au nanoclusters had good dispersion in aqueous solution due to a protecting agent glutathione, and showed a strong orange-red photoluminescence ($E_m = 598$ nm) with high photo-, storage-, metal- and pH-stability (Fig. S3-II†), which was used as a sensing probe for highly sensitive and selective label-free detection of Cu^{2+}.[56] Recently, Aminabhavi *et al.* reported a green synthesis of three-dimensional hexagonal-like zero-valent Cu materials *via* the sonolysis of copper(II) acetate in a medium consisting of ethylene glycol-ethanol (1 : 1),[57] and the resulting nanostructures with high purity (>99%) demonstrated a high efficiency for the reduction of nitrate from polluted waters.

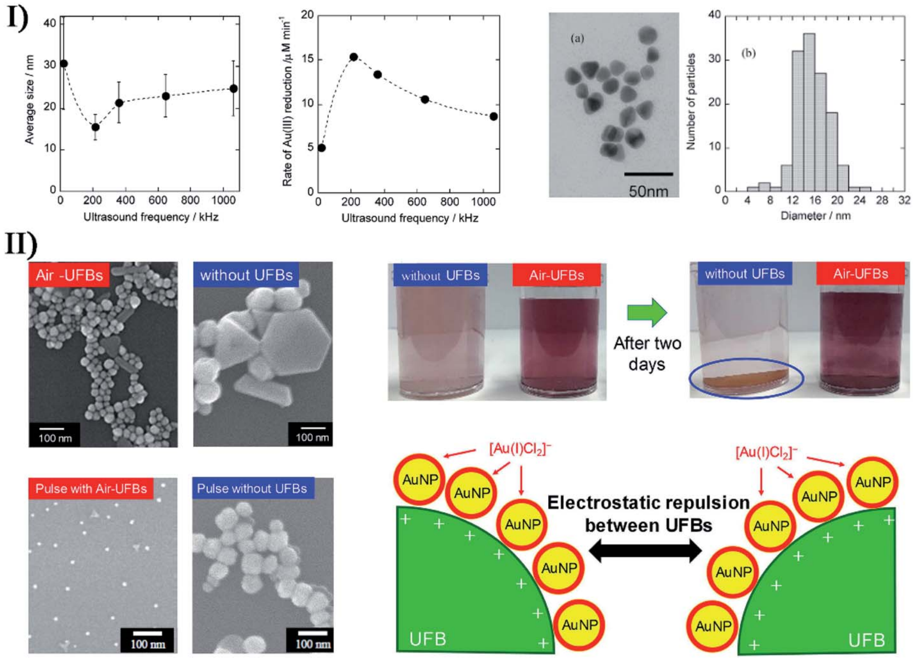

Fig. 5 (I) Left: average size of Au nanoparticles; middle: rate of Au(III) reduction as a function of ultrasound frequency (0.2 mM Au(III), 20 mM 1-propanol, Ar atmosphere, 0.1 W mL^{-1} ultrasonic power), where each error bar corresponds to the standard deviation of the size of Au nanoparticles; right: TEM micrograph (a) and size distribution histogram (b) of Au nanoparticles synthesized after 120 min irradiation with 213 kHz ultrasound; the scale bar is 50 nm in (a). Reproduced with permission from ref. 46. Copyright 2005 American Chemical Society. (II) Left: electron micrographs of spherical Au nanoparticles (AuNPs) synthesized with and without air-UFBs, where the scale bars are 100 nm; right: photographs of AuNPs colloids prepared with and without air-UFBs, and stabilization mechanism of AuNPs colloids containing UFBs. Reproduced with permission from ref. 47. Copyright 2020 Elsevier.

Also, bimetal or alloy nanoparticles have been obtained by an ultrasound-assisted Ostwald ripening process. In the electrocatalysis field, alloy nanoparticles containing Pt have attracted enormous interest not only for their low material cost by reducing the Pt amount, but also for their enhanced catalytic activity, durability and selectivity. By sonicating metal salts in an argon-purged non-aqueous solution containing a strong reducing agent, Gümeci *et al.* prepared bimetallic nanoparticles consistent with Pt_3Ni stoichiometry by adjusting the mole ratio of Pt^{4+} and Ni^{2+} ions.[58] According to both specific activity and mass activity, the activated Pt_3Ni sono-nanoparticles demonstrated a 2–3 times higher oxygen reduction activity than a commercial Pt/C catalyst. To obtain another oxygen reduction electrocatalyst, they later described the synthesis of homogeneous Pt/Cu nanoparticles with the aid of high-intensity ultrasound.[59] Such amorphous, uniformly alloyed nanomaterial showed particle diameters of 2–3 nm, and had a composition consistent with a $PtCu_3$ stoichiometry. Compared with commercial Pt catalysts, the de-alloyed sample exhibited a 3- to 6-fold enhancement in oxygen reduction reaction activity. Wang *et al.* successfully synthesized Au@Pt nanocolloids with nanostructured dendritic Pt shells by chemically reducing both H_2PtCl_6 and $HAuCl_4$ species in a low-concentration surfactant solution,[60] and an ultrasonic treatment dramatically decreased the particle size with a narrower size distribution. As a result of a better reduction potential, Au ions were preferentially reduced over a short time to form Au seeds, followed by the overgrowth of Pt dendritic nanowires on the seeds. By controlling the Pt ions/Au ions molar ratios in the precursor solutions, the thicknesses of Pt shells on Au cores could be tuned easily.

To make toxic mercury (Hg) serve as a safe material in electrochemistry and catalysis fields, Gedanken *et al.* successfully prepared bimetallic Hg/Pd alloys (HgPd 1 : 1, HgPd 2.5 : 1, and HgPd 4 : 1) by sonicating an aqueous Pd(II) nitrate solution with liquid mercury.[61] Hg/Pd catalyst exhibited superior stability and reusability to other noble metal-based catalysts. Later on, they also achieved pure crystalline Hg–Ag amalgam microspheres with uniform morphology by ultrasonically reacting liquid mercury with an $AgNO_3$ aqueous solution (Fig. 6).[62] In the study of Kwon and coworkers,[63] another kind of bimetallic alloy, namely Pd_nM ($n = 1$ for M = Mn, Fe, and Co; $n = 1$, 2, and 3 for M = Ni) nanoparticles, was synthesized on carbon supports by sonochemical catalytic reactions of Pd(acetylacetonate)$_2$ with Ni(acetylacetonate)$_2$, Co(acetylacetonate)$_2$, Mn(acetylacetonate)$_2$ or Fe(acetylacetonate)$_3$ in ethylene glycol. Similarly, trimetallic nanoparticles ((Pd,Co)@Pt) with different elemental compositions have been obtained by the ultrasound-assisted polyol synthesis of Co(acetylacetonate)$_2$, Pd(acetylacetonate)$_2$ and Pt(acetylacetonate)$_2$, where the nanoparticles had a Pt-enriched surface with Pd and Co forming the core.[64] Other sonchemical syntheses of bimetal (*e.g.*, Au/Ag, Au/Pd, Pt/Ru) or even multi-metal nanomaterials (*e.g.*, NiCoPd, Pt/PdNiMo) have been reported as well.[65–68]

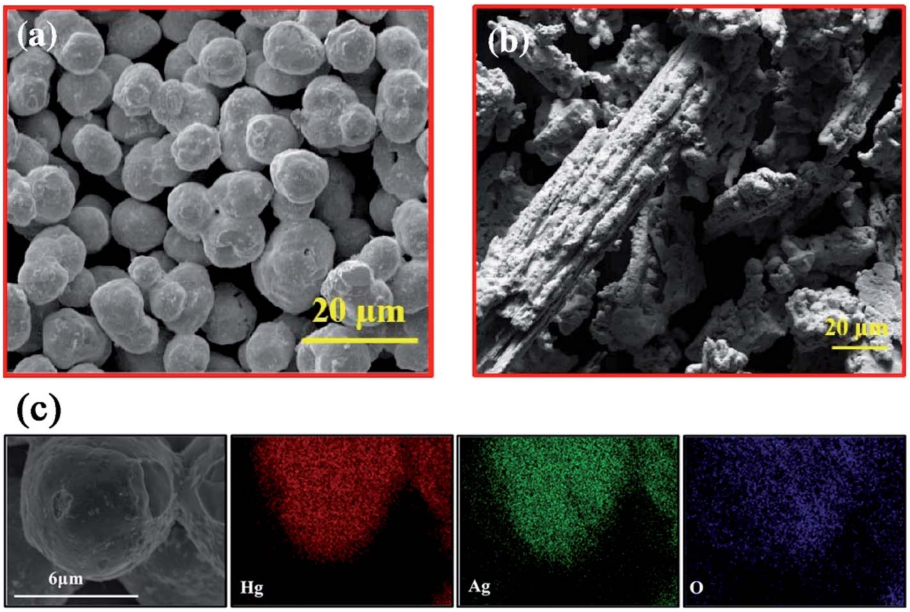

Fig. 6 SEM images of Hg–Ag amalgam with a 1.5 : 1 molar ratio prepared by sonication (a) and stirring methods (b). HRSEM image and elemental mapping (c) of composite Hg : Ag (1.5 : 1). The scale bars are 20 µm in (a) and (b), and 6 µm in (c). Reproduced with permission from ref. 62. Copyright 2018 Elsevier.

5. Metal compounds

Both volatile organometallic compounds and nonvolatile metal precursors are not only limited to the synthesis of nanostructured metals or alloys by sonochemical catalysis or ultrasound-assisted reduction, and various metal compounds including metal oxides, metal hydroxides, metal chalcogenides, metal carbides, *etc.*, can also be prepared from the relevant precursors. Certainly, apart from ultrasound irradiation and reacting precursors, the synthesis processes sometimes involve templates or other technologies.

5.1. Template-free approach

Upon the collapse of bubbles, the high temperature in the localized hotspots can make the reactive metal atoms decompose from metal precursors and react with dissolved gas, other solutes or even solvent molecules, producing metal compounds without any assistance including templates and other structure-directing agents. For instance, $Mo(CO)_6$ in hexadecane by sonochemical heating under CH_4/H_2 gas could cause the formation of nanostructured Mo_2C porous aggregates,[69] and iron nitride nanoparticles have been produced when the ultrasound treatment of iron carbonyl compounds occurred under a reductive NH_3/H_2 gas mixture.[70] Recently, Argirusis and coworkers sonochemically prepared metal oxide nanoparticles on anode materials from organic solvents containing $W(CO)_6$ or $Mo(CO)_6$ in 80 °C ambient air.[71] They found that ultrasound intensity and solvents were responsible for the size distribution and morphology of resultant nanoparticles when the ultrasound intensity/duration as well as the ratio of precursor/substrate compounds affected the decoration loading extent of nanoparticles on substrates.

For metal oxides or hydroxides, the sonication of metal salts in an aqueous solution is a typical synthesis method in the presence of oxygen sources (*e.g.*, air, oxygen gas or hydroxides). Using sonication, Price *et al.* produced copper oxide nanoparticles from a copper acetate and hydrogen peroxide solution, or obtained zinc oxide nanoparticles from a zinc acetate and NaOH solution.[72] Uzunov *et al.* utilized different methods (*i.e.*, precipitation, mechanochemical treatment and sonochemical process) to prepare nano-sized zinc oxides, and three products had various morphologies with a crystallite size below 20 nm.[73] Interestingly, the ZnO nanorods from the sonochemistry-assisted process exhibited the highest photocatalytic activity for the degradation of malachite green under UV irradiation, and the polycrystalline zinc oxide from the precipitation-assisted process had a better photocatalytic efficiency under visible irradiation, but on the contrary, the nano-sized ZnO from the mechanochemistry-assisted process had lower photocatalytic activity because of the inhomogeneous size distribution.

Spinel ferrites are promising magnetic materials and widely used in various fields, so lately, the sonochemical syntheses of novel spinel ferrite nanostructures have become an active research area.[74–78] For example, Almessiere, Slimani and coworkers produced a series of high-purity spinel ferrite compositions *via* ultrasonic irradiation, such as $Mn_{0.5}Zn_{0.5}Eu_xDy_xFe_{1.8-2x}O_4$ ($x \leq 0.1$), $Mn_{0.5}Zn_{0.5}Fe_{2-2x}(Dy_xY_x)O_4$ ($0.0 \leq x \leq 0.05$), $Ni_{0.3}Cu_{0.3}Zn_{0.4}Tm_xFe_{2-x}O_4$ ($0.0 \leq x \leq 0.10$), $CoTb_xFe_{2-x}O_4$ ($0.00 \leq x \leq 0.10$), $CoTm_xFe_{2-x}O_4$ ($0.0 \leq x \leq 0.08$), $Co_{0.7}Zn_{0.3}Tm_xFe_{2-x}O_4$ ($0.0 \leq x \leq 0.04$), *etc.*[79–93] They examined the structural properties, morphological properties, and physical properties (*e.g.*, magnetic traits, optical traits, and electrical traits) of the products, and even evaluated their biological characteristics for potential anti-cancer and anti-bacterial activities. Additionally, they also utilized ultrasonic-assisted approaches to prepare many ferromagnetic M-type hexaferrites including $BaTm_xTb_xFe_{12-2x}O_{19}$ (x = 0.00–0.05) hexaferrites, $Ba_{0.5}Sr_{0.5}Nd_xEu_xFe_{12-2x}O_{19}$ (x = 0.00–0.05) hexaferrites, $Sr_{0.5}Ba_{0.5}Tm_xSm_xFe_{12-2x}O_{19}$ (x = 0.00–0.05) hexaferrites, $Sr_{0.5}Ba_{0.5}Tm_xTb_xFe_{12-2x}O_{19}$ (x = 0.00–0.05) hexaferrites, and so on.[94–98]

Metal chalcogenides can be obtained by the sonication of metal salts and chalcogen sources (*e.g.*, thiourea for sulfur source, selenourea for selenium source, or others). Suslick *et al.* ultrasonically irradiated $Mo(CO)_6$ and elemental sulfur in 1,2,3,5-tetramethylbenzene under argon gas, producing clustered MoS_2 nanoparticles with a high edge surface area, and the product exhibited substantially high catalytic activity for the hydrodesulfurization of thiophene.[99] To develop a viable non-enzymatic electrochemical sensor for H_2O_2 detection, Chen *et al.* prepared a smooth grass-like vanadium disulfide from VCl_3 and Na_2S precursors through a simple sonochemical method without surfactants or templates.[100] The grass-like structure was comprised of a large number of randomly oriented leaf-like flakes which had an average diameter of 250 nm and a thickness of 60 nm (Fig. S4†), and there were no significant impurities but vanadium (V) and sulfur (S) elements with a 1 : 2 atomic ratio.

In a recent study by Park *et al.*, a substantially green procedure was designed to yield $Cu(In_{0.7}Ga_{0.3})Se_2$ nanoparticles on the basis of a slightly modified sonochemical method.[101] The reaction was carried out at room temperature with ethanol as the only solvent, $NaBH_4$ as a reducing agent, and a 5 h ultrasound irradiation. In the reaction pathways, ultrasound irradiation played an important role in decomposing the intermediate Cu_2Se, so prolonging the sonication time would result in the formation of $Cu(In_xGa_{1-x})Se_2$ compounds with much better crystallinity, and wherein a 5 h sonication yielded tetragonal $Cu(In_{0.7}Ga_{0.3})Se_2$ nanocrystals without any Cu_2Se crystals. In order to develop an electrocatalyst for the effective sensing of diphenylamine, Chen *et al.* prepared ytterbium-doped molybdenum selenide ($YbMoSe_2$) by using a one-step ultrasonic method.[102] $YbMoSe_2$ displayed a densely packed hierarchical sheet-like or flower-like structure with uniform shape and size (Fig. 7), and there was a mixing and disordered arrangement in the atomic crystal lattice due to the substitution of Yb with $MoSe_2$. In the hexagonal lattice structure of $YbMoSe_2$, the lattice spaces of Yb and $MoSe_2$ were 0.6 nm assigned to the (002) plane, and lattice distortion/defects on the $MoSe_2$ crystal lattice occurred due to the exposed lattice plane of Yb into the atomic lattice of $MoSe_2$.

Other metallic compounds can also serve as element or ligand sources for the ultrasound-aided synthesis of metal

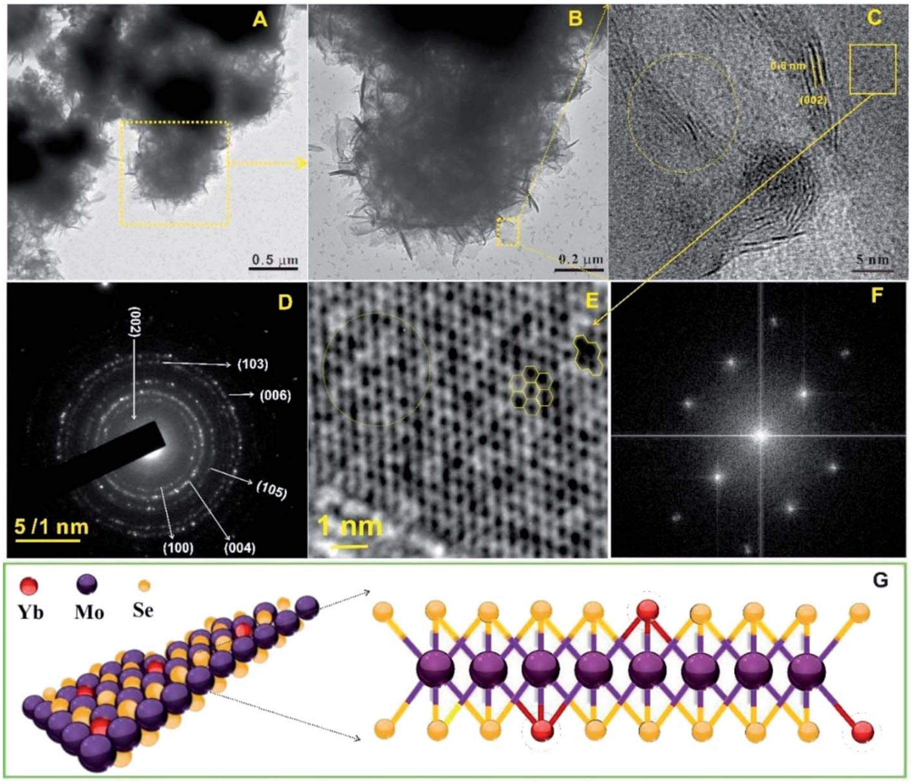

Fig. 7 TEM images ((A) scale bar = 0.5 μm; (B) scale bar = 0.2 μm), HRTEM image ((C) scale bar = 5 nm), and selected area electron diffraction pattern ((D) scale bar = 1 nm) of layered $YbMoSe_2$. Fast Fourier transform pattern of $YbMoSe_2$ ((E) scale bar = 1 nm), and selected area electron diffraction pattern in the case of basal plane of $YbMoSe_2$ (F). Schematic diagram of $YbMoSe_2$ (G). Reproduced with permission from ref. 102. Copyright 2019 Elsevier.

compounds. Kipcak *et al.* used magnesium chloride hexahydrate and different boron sources (borax, tincalconite, boric acid, and boron oxide) as the precursor materials to synthesize magnesium borate by sonochemistry-assisted routes, and all the outcomes were $MgO(B_2O_3)_3 \cdot 7H_2O$ with high crystallinity and higher than 80% yields.[103] Pinkas and coworkers utilized a sonochemical precipitation method to form insoluble amorphous uranium phosphates from UO_2^{2+} precursors in trialkyl phosphate solutions.[104] In this sonolysis experiment, the high-boiling trialkyl phosphates served as a phosphate source to create some active species by the decomposition of ester molecules and then reacted with uranium precursors in the solution, followed by the obtained amorphous precipitates changing into crystalline uranium diphosphate (UP_2O_7) when heated to 1000 °C. The efficiency of uranium removal was higher than 30% by sonochemical precipitation, which might become a potential remote separation technology for uranium in waste streams.

Mastai *et al.* described a surfactant-free sonochemical method to synthesize $CoFe_2O_4$ nanoparticles for the catalytic degradation of elastomer-based polymers, where $Co(CH_3COO)_2$ and $Fe(C_5H_7O_2)_3$ were sonicated in a slightly basic solution (pH = 8) at 75 °C.[105] After calcination at 500 °C, such cobalt ferrite nanoparticles demonstrated an average particle size of around 27 ± 6 nm. Salavati-Niasari *et al.* synthesized pristine uniform $DyVO_4$ nanoparticles by a sonochemical method (60 W, 18 kHz) so as to create a highly efficient photocatalyst for water treatment.[106] Since the selective adsorption of surfactants on the crystal facets could control the growth rates along the different crystal directions due to the anisotropy in adsorption stability, the researchers conducted a size and uniformity repair of nanomaterials through using different types of surfactants such as anionic surfactants, cationic surfactants and nonionic surfactants. They found that cetyltrimethylammonium bromide could be used to prepare optimum $DyVO_4$ nanoparticles with suitable uniformity and small sizes. Later in the presence of PEG-6000, they synthesized pure $Zn_{0.35}Fe_{2.65}O_4$ nanostructure as a ferrite catalyst material by sonicating $Fe(NO_3)_3$ and $Zn(OAc)_2$ in a basic aqueous solution, aiming to purify waste water containing different pollutants.[107] In the report of Ashiri *et al.*,[108] the sonochemical catalysis approach was used for the synthesis of $BaTiO_3$ nano-powders from titanium tetrachloride, barium(II) chloride, and sodium hydroxide in an aqueous solution. The results were contrasted with those of a mechanochemical method, demonstrating that the sonochemical synthesis allowed the preparation of highly pure tetragonal $BaTiO_3$ at a much lower temperature and a shorter time span, because the reactant ions in the solution mixture would homogenously enter into the perovskite structure in order.

5.2. Template-directing approach

In the sonication process, an appropriate structure-directing agent or removable template can serve to create different nanostructured materials. To make one-dimensional ZnO nanorods and two-dimensional ZnO nanoflakes, Vabbina *et al.* deposited vertically aligned nanostructures on Au-coated Si substrates by sonicating a zinc salt, in which hexamethylenetetramine was used as a shape-directing agent to attach to the nonpolar facets of ZnO and allow the growth only in the ⟨0001⟩ direction.[109] Under an ammonia condition, Zhu *et al.* sonochemically reacted $CdCl_2$ with $NaSeSO_3$ producing hollow spherical assemblies composed of CdSe nanoparticles,[110] where amorphous $Cd(OH)_2$ from the hydrolysis acted as an *in situ* template to direct the growth of CdSe nanoparticles and the formation of spherical assemblies. Chu *et al.* fabricated coupled twin-shaped hollow hemispherical calcium molybdate microstructures *via* a facile ultrasound-assisted approach at room temperature,[111] where ethylenediaminetetraacetic acid as a structure-directing agent played pivotal roles in the formation of unique architecture on the basis of the oriented attachment and subsequent Ostwald ripening mechanism (Fig. S5†). The coupled twin-shaped hollow hemispheres had high specific surface area, hollow interior, mesoporous structure and low density.

Expectedly, SiO_2 materials or carbon nanoparticles usually give an aid to directly depositing produced free metal atoms onto a support, forming various micro-/nano-structures. Under air, Suslick *et al.* carried out the ultrasound irradiation of $Mo(CO)_6$ and silica nanoparticles in 1,2,3,5-tetramethylbenzene, and the MoO_3-coated silica nanoparticles as the pre-product would form hollow MoO_3 when using HF to etch the silica component (Fig. 8-I).[112] Similarly, hollow MoS_2 could be yielded by replacing air with Ar gas and adding sulfur into the system.[51] In another study, Suslick *et al.* prepared nanosized hollow hematite from the precursor $Fe(CO)_5$ when carbon nanoparticles created from polypyrrole carbonization were employed as a sacrificial template (Fig. 8-II).[113] Also, Yang *et al.* obtained porous Co_3O_4 from the sonochemical product of $Co_4(CO)_{12}$ with carbon nanotubes as a template which spontaneously removed itself *via* combustion attributed to the rapid oxidation of elemental Fe upon air exposure (Fig. 8-III).[114] During the sonochemical synthesis of nanostructured $PbWO_4$, Zhu and coworkers realized the control of unique morphologies in the presence of soft templates.[115] Sonicating a mixed solution containing $Pb(CH_3COO)_2$, $NaWO_4$ and P123 (Pluronic block copolymer) would result in the formation of hollow metal oxide spindles (Fig. 8-IV), but only solid particles were obtained in the absence of ultrasound. This could probably be attributed to the proposal that ultrasound irradiation changed P123 micelles into micelle aggregates with a hollow spindle structure.

5.3. Technology-cooperating approach

In cooperation with other approaches, ultrasound irradiation is capable of enabling the preparation of more metal compound nano-/micro-structures. To decrease the sintering temperature in the preparation of strontium hexaferrite ($SrFe_{12}O_{19}$) nanoparticles, Jesús and Miró described a synthesis route of sonochemistry and annealing.[116,117] The sonochemical process yielded an amorphous phase containing Fe^{3+}, Fe^{2+} and Sr^{2+} ions from a complexed polyol solution of metallic acetates, and the

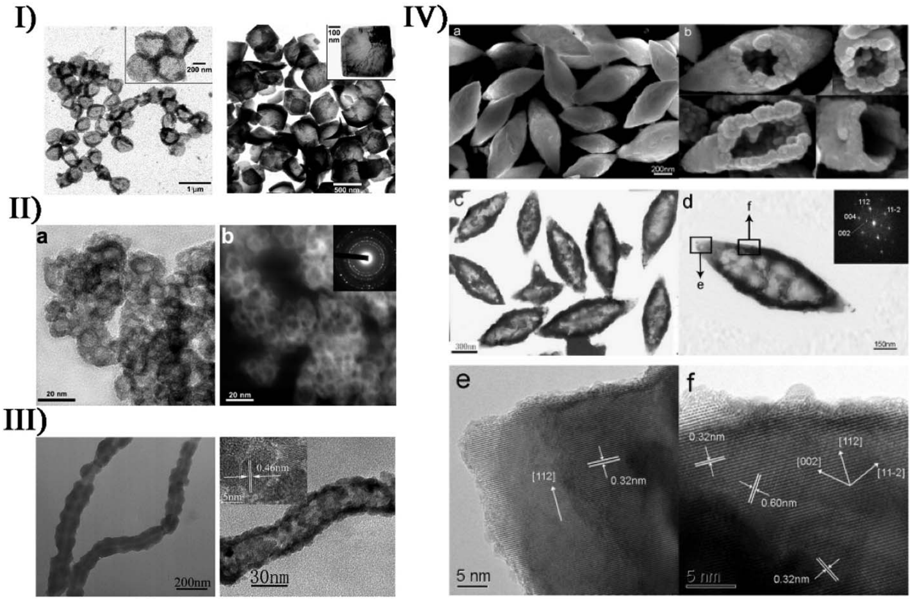

Fig. 8 (I) TEM micrographs of sonochemically prepared hollow MoO_3 nanospheres from HF etching of MoO_3/SiO_2 before thermal annealing (left: scale bar = 1 μm) and after thermal annealing at 350 °C (right: scale bar = 500 nm), where insets are at higher magnification (left: scale bar = 200 nm; right: scale bar = 100 nm). Reproduced with permission from ref. 112. Copyright 2005 American Chemical Society. (II) Bright-field TEM image ((a) scale bar = 20 nm) and dark-field TEM image ((b) scale bar = 20 nm) of nanosized hollow iron oxide (inset: SAED pattern). Reproduced with permission from ref. 113. Copyright 2007 American Chemical Society. (III) TEM images (left: scale bar = 200 nm; right: scale bar = 30 nm) of CNTs–CoO_x nanocables prepared by sonication and Co_3O_4 nanotubes after the calcination of CNTs–CoO_x nanocables, where the upper-left inset corresponds to the HRTEM image (scale bar = 5 nm). Reproduced with permission from ref. 114. Copyright 2007 Wiley. (IV) Typical SEM image ((a) scale bar = 200 nm) of as-prepared $PbWO_4$ sample, (b) SEM images of several broken hollow spindles viewed from different angles, and typical TEM image ((c) scale bar = 300 nm), SAED pattern ((d) scale bar = 150 nm), and HRTEM images recorded on the tip ((e) scale bar = 5 nm) and the shell ((f) scale bar = 5 nm) of a hollow spindle. Reproduced with permission from ref. 115. Copyright 2006 American Chemical Society.

annealing of the amorphous phase caused the generation of hexagonal $SrFe_{12}O_{19}$ by the creation and phase conversion of intermediates. Moreover, high output power and long time (up to 3 h) of sonication could promote the crystallinity of amorphous phases, decrease in crystal size, and modify the morphology of particles. Similarly, Cavalcante and coworkers synthesized triclinic-structured tungstate ($CuWO_4$) crystals by a sonochemical approach and a subsequent heat treatment in a conventional furnace.[118] Within the sol–gel preparation of nanostructured metal compounds, ultrasound irradiation can accelerate the hydrolysis process, improve the phase purity, and create products with a narrower size distribution and a higher surface area. Yu *et al.*, Mansour *et al.* and Haridas *et al.* separately produced TiO_2 nanoparticles by the sonochemical hydrolysis of titanium tetra-isopropoxide precursor.[119–121] In these synthesis cases, the accelerated hydrolysis in sonication improved the crystallinity of TiO_2, showing the significant effects of ultrasound irradiation on the microstructure and crystallization kinetic mechanism of amorphous TiO_2. In the report of Chen *et al.*, differently, rod-like ZnO nanocrystallites were synthesized from zinc acetate *via* an ultrasound-assisted non-hydrolytic sol–gel process,[122] in which the reactant diethylene glycol acting as a capping agent limited particle growth and prevented agglomeration. The final ZnO nanorods had a width of about 30 nm and length of 50–70 nm. To obtain thin ZrO_2 layers on structured reactors, Jodłowski developed an efficient ultrasound-assisted sol–gel method through the synergistic combination of three processes:[123] sonochemical synthesis of Zr sol–gel from a Zr(IV) precursor solution, addition of ethylene glycol and glycerol as stabilizing agents, and deposition of ZrO_2 on FeCr alloy supports. The resultant ZrO_2 films on the metallic structure were dense and uniform without any impurities.

Furthermore, many technologies such as sono-fragmentation and ultrasonic spray pyrolysis have been developed to produce nanostructured materials on account of the physical or mechanical effects from the ultrasound.[124] In sonication, few-layered materials such as $MoSe_2$, MoS_2, WS_2 and Bi_2Te_3 can lead to single-layered nanosheets by direct liquid-phase exfoliation, which is actually a response from sono-fragmentation.[125] Suslick *et al.* have prepared MnO_2 microspheres *via* an ultrasonic spray pyrolysis process, where a $KMnO_4$ and HCl mixed solution was nebulized into micro-sized droplets serving as a microreactor and produced microspheres upon heating.[126] By tuning the precursor concentrations and furnace temperatures, the microsphere morphology could be controlled. For instance, the synthesis yielded amorphous MnO_2 microspheres at 150 °C but crystalline α-MnO_2 at 500 °C. In the study of Skrabalak *et al.*,[127] ultrasonic spray pyrolysis coupled with a molten salt synthesis successfully produced single-crystalline hexagonal $NaInS_2$ nanoplates with an average diameter of 572 ± 175 nm and a width of 51 ± 16 nm, and the

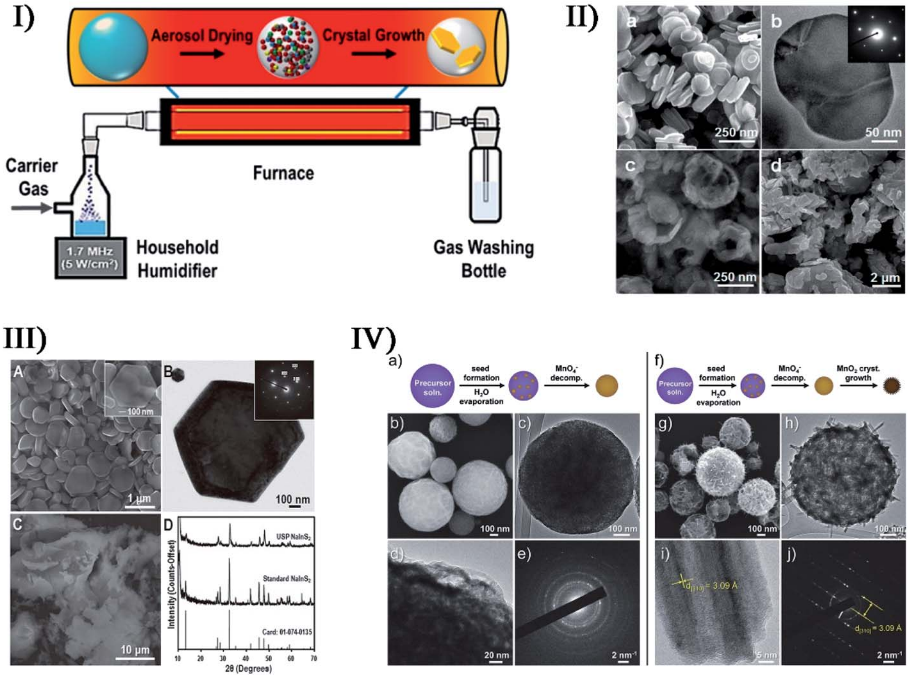

Fig. 9 (I) Simple reactor schematic for ultrasonic spray synthesis (USP). Reproduced with permission from ref. 128. Copyright 2017 American Chemical Society. (II) SEM image ((a) scale bar = 250 nm) and TEM image ((b) scale bar = 50 nm) of $NaSbO_3$ at 900 °C, where the inset in (b) displays the corresponding SAED pattern, and for comparison, SEM images of $NaSbO_3$ product obtained from an aerosol-assisted synthesis without $CsNO_3$ flux ((c) scale bar = 250 nm) and $NaSbO_3$ prepared from conventional solid-state synthesis ((d) scale bar = 2 μm). Reproduced with permission from ref. 129. Copyright 2015 American Chemical Society. (III) SEM image ((A) scale bar = 1 μm) and TEM image ((B) scale bar = 100 nm) showing the hexagonal shape of $NaInS_2$ nanoplates produced *via* USP (the inset electron diffraction pattern in (B) demonstrates the single-crystalline nature); SEM image ((C) scale bar = 10 μm) of $NaInS_2$ prepared through a non-USP method for comparison, and (D) X-ray diffraction patterns of the USP and non-USP materials. Reproduced with permission from ref. 127. Copyright 2012 Wiley-VCH. (IV) Morphology of MnO_2 microspheres produced *via* USP at 150 °C (a–e) and 500 °C (f–j) ((b, c, g and h) scale bars = 100 nm; (d) scale bars = 20 nm; (e and j) scale bars = 2 nm; (i) scale bars = 5 nm); TEM images (c, d, h and i) where increasing the reaction temperature caused the formation of larger crystals; SEM images (b and g); and electron diffraction patterns (e and j). Reproduced with permission from ref. 126. Copyright 2015 Wiley-VCH.

photoanode films fabricated from the $NaInS_2$ nanoplates provided nearly 25 times greater photocurrent upon illumination than films made with traditional $NaInS_2$. Later in order to develop a facile and general synthetic strategy for particles with size, shape and compositional control, they described a simple reactor for ultrasonic spray synthesis,[128] where the particle formation occurred within spatially and temporally confined droplets. By such a step-by-step procedure, $AgSbO_3$ visible-light photocatalysts were synthesized when single-crystalline $NaSbO_3$ nanoplates prepared by salt-assisted aerosol combustion were used as a topotactic template.[129] Fig. 9 shows ultrasonic spray pyrolysis creating some nano- and micro-materials.

6. Non-metal materials

Apart from metals, alloys, and metal compounds, nonmetal nanomaterials can be also facilely produced by sonochemical effects or ultrasound-assisted technologies, mainly covering carbon materials and non-carbon materials.

6.1. Carbon materials

Based on the physical/chemical effects of ultrasound, single- and few-layered materials are often prepared by breaking 3D layer structures down to 2D planar structures, where the attractive forces between individual layers are completely overcome. As a typical case, the synthesis of graphene oxide (GO) using Hummers' method is widely employed and admirable: oxidization of pristine graphite increases the interlayer distance and consequently weakens the van der Waals force relative to graphite, so that a bath or horn sonication facilitates the exfoliation of single- or few-layered GO from the bulk material. Sagadevan *et al.* synthesized perfectly crystalline GO by a modified Hummers' method utilizing a sonochemical technique,[130] and the sample was wanted specifically for the design of smart opto-electronic devices. However, the presence of oxides (*i.e.* epoxy bridges, hydroxyl groups, and carboxyl groups) would disrupt the band structure and completely degrade the electronic properties, though the oxides could be removed by a reduction step. In another study, Lee *et al.* reported the synthesis of high-purity reduced GO (rGO) from pristine graphite *via* a one-step ultrasonic reduction method,[131] where the processes avoided the harsh reaction conditions including high temperature and highly toxic hydrazine. The as-synthesized rGO exhibited a very thin wrinkled paper-like structure with sheet folding, where minimal layers were about 4 layers with a layer spacing of about 1 nm.

Sonication-assisted liquid-phase exfoliation methods can allow the extraction of low-defect graphene materials (Fig. 10-I).[132] Coleman *et al.* successfully utilized the direct exfoliation of graphite in *N*-methylpyrrolidone by sonication to produce single- and few-layered graphene (a monolayer yield of about 1 wt%), where the surface energy between solvent and graphite had to match (about 40 mJ m^{-2}) to obtain high-yield exfoliated graphene without defects or oxides.[133] Romero-Salguero *et al.* reported another ultrasound-assisted liquid-phase exfoliation method to synthesize graphene nanosheets from microcrystalline graphite powder in *o*-dichlorobenzene,[134] and the resulting nanostructures were demonstrated to be unfunctionalized, non-oxidized and isolated. Trusova's group developed the synthesis of oxygen-free graphene sheets by the sonochemical exfoliation of graphite powder in *N*,*N*-dimethyloctylamine-aqua medium (pH was equal to 3),[135] followed by the fixation of graphene sheets at the organic-aqua interface (Fig. 10-II). In order to avoid the commonly used organic exfoliating solvents, Yusoh and coworkers used a commercial coffee as a green medium to facilely create few-layer graphene flakes in sonication (Fig. 10-III).[136] However, there was a large presence of hydroxyl groups in the graphene, which was different from the other ultrasound-assisted liquid-phase exfoliations, suggesting that the graphene was successfully functionalized by the active chlorogenic acid in coffee.

Other nonmetal materials, such as carbon nanotubes, graphene quantum dots, carbon nanodots, and black phosphorus quantum dots, can be prepared from corresponding precursors by ultrasonic treatment as well. Ha and Jeong reported a sonochemical route to prepare crystalline multi-walled carbon nanotubes,[137] in which ultrasound was used to irradiate a *p*-xylene solution containing silica powder and ferrocene. The *p*-xylene acting as a carbon source was pyrolyzed to carbon atoms or moieties *via* the catalysis of Fe clusters that originated from the sonochemically decomposed ferrocene, and finally created high-purity multi-walled carbon nanotubes. The nanotube wall thickness was in the range of 25–40 nm and consisted of 10–30 graphitic walls. Kumar *et al.* made carbon nanodots from poly(ethylene glycol) in sonication, forming a coating layer of carbon nanodots on polyethylene.[138] The samples had an average diameter of 2–9 nm depending on the preparation conditions, and showed good fluorescence properties because the highest quantum yield of emission was about 16%. Similarly, many other carbon sources can also be subjected to ultrasonic treatments to prepare carbon dots or doped nanodots. Li *et al.* used alkali- or acid-assisted ultrasonic treatment of glucose to obtain carbon dots, while Wei *et al.* developed a facile sonochemical method to make nitrogen-doped carbon dots by using the pyrolysis of carbon precursors (citric acid and ethylene diamine).[139–141] Recently by sonicating dopamine in dimethylformamide, Zhou *et al.* fabricated nitrogen-doped carbon quantum dots with temperature-dependent fluorescence.[142] The product had superior dispersibility and stability in water, strong and stable fluorescence against various pH and ionic strengths, low cytotoxicity, and high photostability, as well as exhibiting a sensitive quenching phenomenon towards Fe^{2+} ions.

6.2. Non-carbon materials

In recent years, many non-carbon materials have been also produced by sonochemical catalysis technologies. In the absence of any templates or surfactants, Xia *et al.* employed the

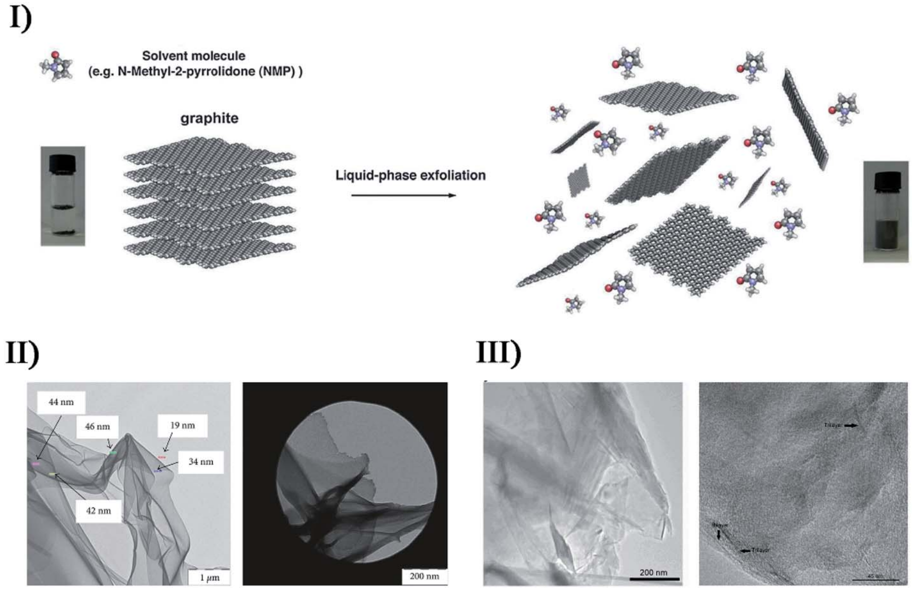

Fig. 10 (I) Schematic representation of the liquid-phase exfoliation process of graphite in the absence of surfactant molecules. Reproduced with permission from ref. 132. Copyright 2014 Royal Society of Chemistry. (II) TEM micrographs (bright field: scale bar = 1 μm; dark field: scale bar = 200 nm) of graphene films obtained from the decanted liquid substance after graphene-containing colloid sedimentation during 12 h. Reproduced with permission from ref. 135. Copyright 2018 Hindawi. (III) TEM images of GC (left: scale bar = 200 nm), and at higher magnification with the presence of bilayer and trilayer graphene (right: scale bar = 40 nm) with very similar orientations to each other. Reproduced with permission from ref. 136. Copyright 2019 Elsevier.

sonication of amorphous selenium colloids in alcohol to thermodynamically form trigonal selenium (t-Se) nanowires *via* a solid-solution-solid transformation mechanism,[143] where selenium nanocrystals were sonochemically nucleated in a trigonal structure acting as the seeds of the nanowires. Different from Xia's work, Li *et al.* used a longer ultrasonication time (40 kHz, 100 W cm^{-2}) to synthesize single-crystalline t-Se nanotubes and nanowires.[144] When the sonication period was prolonged to 30–60 min, Se nanotubes were initially formed from the spherical-like t-Se seeds and gradually grew within the aging time. With the aging time being prolonged to 24 h, the t-Se nanotubes grew into a well-organized shape with diameters of less than 200 nm, whereas the tubular structure tended to collapse and change into t-Se nanorods and nanowires with diameters of 20–50 nm after further aging.[144] The two stages could not be separated obviously. Salavati-Niasari *et al.* sonochemically synthesized Se nanostructures by using $SeCl_4$ as a new precursor in a reducing environment.[145] When the ultrasonic power was set at about 60 W with a 30–40 min period, the sufficient amounts of energy produced Se nanosheets with an average diameter of 200 nm; if the stronger reducing agent potassium borohydride instead of hydrazine was used in the synthesis, it did not create Se nanosheets but Se nanoparticles with an average particle size of 20 nm. Besides, solvent, acid or base environment, and surfactant also played a key role in controlling the morphology and particle size of resultant Se nanostructures. Similarly, they obtained rod-like Se nanostructures by a sonochemical route using thioglycolic acid as the reducing agent.

In the study by Bedini *et al.*, isolated silicon nanoparticles were sonochemically synthesized by Si_3H_8 solution undergoing a sonication process (26 kHz, 10–40 °C) in an inert N_2 atmosphere.[146] The whole formation was mainly attributable to the interplay between the extreme conditions during the bubble collapse and the high density of active species (*e.g.*, silicon radicals) created at such spatially localized points (Fig. S6†). Therein, the incomplete diffusion during the short-lived collapse caused residual bonded hydrogen existing in the particles, and the silicon matrix did not have an enough interaction time to reconstruct into a crystalline state, so the as-synthesized silicon nanoparticles were discrete, hydrogenated, and amorphous. The size of silicon samples was tunable within a 1.5–50 nm range by varying the ultrasound amplitude or the trisilane concentration, where low-amplitude ultrasound or low-concentration Si_3H_8 favored the creation of discrete and monodisperse silicon nanoparticles (size distribution of 2.96 ± 0.82 nm) probably attributed to the smaller microbubbles and/or less trisilane in-diffusion during bubble growth.[133]

Silica (SiO_2) nanoparticles occupy a significant position in scientific research due to their potential applications (*e.g.*, pharmaceuticals, catalysis, pigments, stabilizers, polishing, and sensors), and sonochemical catalysis has extended to the synthesis of various SiO_2 nanostructures. *Via* an ultrasound-assisted sol–gel method, Kim *et al.* successfully prepared monodisperse and size-controlled silica particles with a uniformly spherical shape from tetraethyl orthosilicate in the presence of ammonia.[147] The average diameters of the silica particles were distributed in the range from 40 to 400 nm, and could be controlled by the reactants' molar ratio which determined the nucleation and growth rates of particles. Salavati-Niasari *et al.* also synthesized spherical SiO_2 nanoparticles by the sonochemical method,[148] and, dissimilarly, Schiff-bases (*i.e.*, bis(acetylacetonato)propylene-1,3-diimine and bis(acetylacetonato)buthylene-1,4-diimine) acted as capping agents for the hydrolysis of tetraethyl orthosilicate in aqueous alcohol solution. The molar concentration of Schiff-base ligand could be effective in control of particle size, but the conclusions for bis(acetylacetonato)propylene-1,3-diimine and bis(acetylacetonato)buthylene-1,4-diimine were inconsistent, which was not further explained. Sankar *et al.* reported the

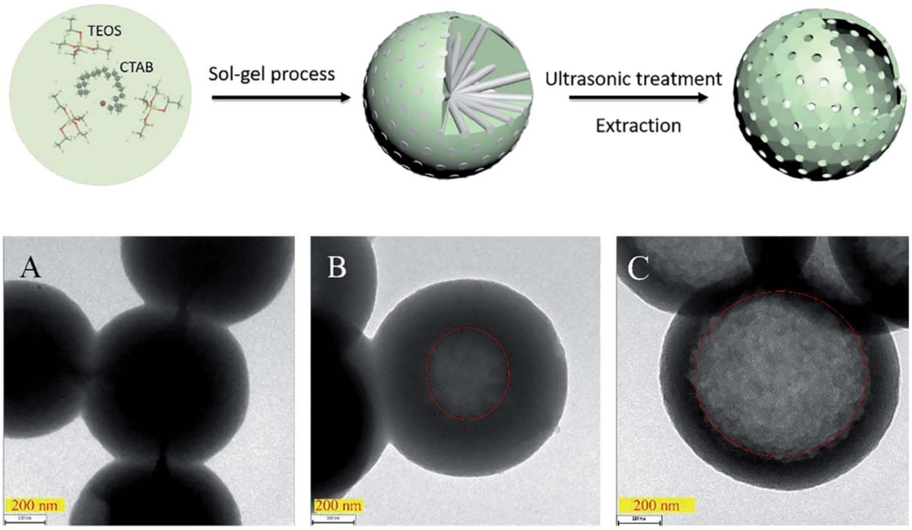

Fig. 11 Conceptual demonstrations of the preparation process of hollow mesoporous silica spheres, where TEM images (scale bars = 200 nm) show the silica spheres prepared at 20 kHz for (A) 2 h, (B) 6 h, and (C) 48 h. Reproduced with permission from ref. 150. Copyright 2019 Elsevier.

synthesis of amorphous silica nanoparticles from brown rice husk *via* the sonochemical process,[149] where the sonication time was varied so as to modulate the product's properties. By increasing the sonication time (0–50 min), the mean particle sizes were facilely controlled from 5 to 40 nm while the pore volumes were changed from 176.33 $m^2 g^{-1}$ to 226.56 $m^2 g^{-1}$, and moreover, the band-gap energy was decreased from 5.77 eV to 5.68 eV. In the study of Jiang *et al.*,[150] a facile ultrasonic-assisted approach was presented to prepare hollow mesoporous silica. Prior to the hollow mesoporous structure, a whole solid was obtained through CTAB-directed sol–gel processes, and then a one-step ultrasonic treatment was conducted acting as a selective etching. Fig. 11 exhibits the conversion process of the whole solid to hollow structure for different ultrasound durations.

7. Inorganic composites

Sometimes, the attributes of a single material cannot satisfy some specific demands in a proposal, or it is not able to serve as a qualified candidate for some harsh processes or reactions. Hence, the merging or synergy between elements or materials is a superior choice on the basis of various properties including low cost, high activity, good stability, and so on. So far, nano/micro inorganics have passively formed thousands of combinations for actual requirements, and here, as a highlight, are only provided the hybrid incorporations from metals, metal compounds, and non-metal materials *via* sonication. Sonochemical catalysis represents a feasible, facile and short-time approach for the synthesis of hybrid inorganic materials.

7.1. Metal/metal compounds

On the basis of surface plasmon resonance, a series of hybrid noble metal/metal compounds can be developed to decompose various organic pollutants as plasmonic catalysts. Cho *et al.* produced Ag/AgCl nanocubes with Ag nanoparticles embedded into the AgCl cubic matrices when sonicating sodium chloride, silver nitrate and poly(vinyl pyrrolidone) in ethylene glycol (Fig. 12-I).[151] Such Ag/AgCl nanocrystals had a 115 nm edge length, and their sizes and size distribution could be well controlled by changing the Ag^+ and poly(vinyl pyrrolidone) concentrations in the precursor solutions. Under ambient conditions, the as-obtained Ag/AgCl hybrids displayed an enhanced photocatalytic performance under visible light. Later, Bao *et al.* synthesized Ag/AgX (X = Cl, Br) plasmonic photocatalysts *via* a facile one-pot ultrasonic spray pyrolysis method,[152] wherein $AgNO_3$ and KCl (or KBr) separately worked as Ag source and Cl (or Br) source with no additional conditions (*e.g.*, high pressure), surfactants and reducing agents. Through the thermal decomposition of residual $AgNO_3$ solution, metallic Ag particles uniformly nucleated and covered the surface of AgX grains, becoming an up- and down-structure like a sequence of

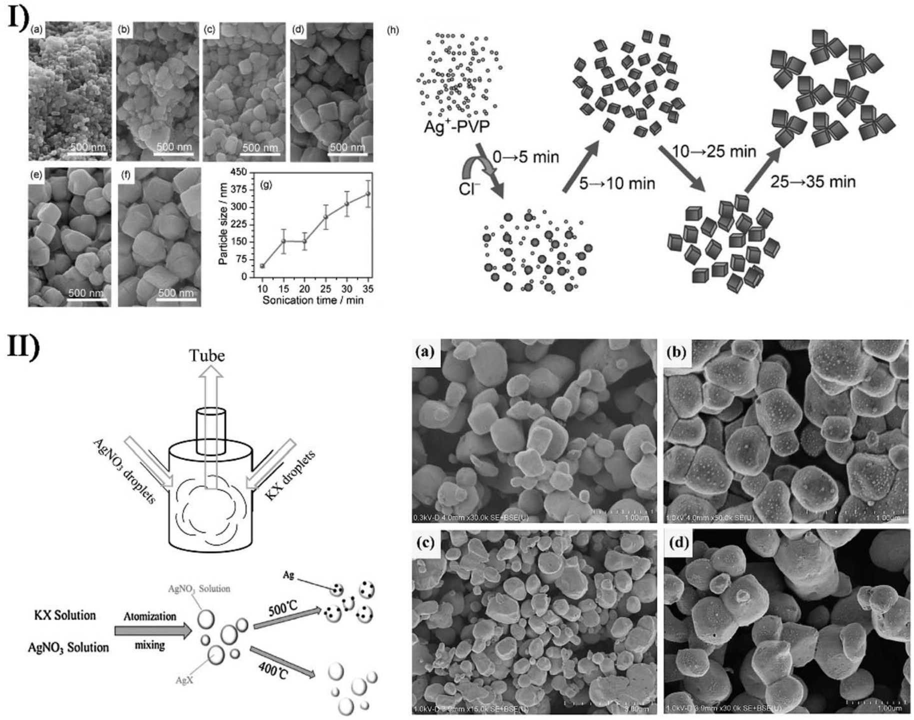

Fig. 12 (I) SEM images (scale bars = 500 nm) of Ag/AgCl nanocrystals at various stages with sonication durations of (a) 10 min, (b) 15 min, (c) 20 min, (d) 25 min, (e) 30 min, and (f) 35 min. (g) Plot of the particle size of AgCl nanocrystals as a function of sonication time (poly(vinyl pyrrolidone) = 20 g L^{-1}, $[Ag^+] = 0.05$ mol L^{-1}). (h) Schematic growth process of AgCl nanocrystals under sonication conditions. Reproduced with permission from ref. 151. Copyright 2012 Wiley. (II) Schematic diagram of experimental setup, illustrating the preparation process of Ag/AgX (X = Cl, Br) photocatalyst, and SEM images of (a) AgCl, (b) Ag/AgCl, (c) AgBr, and (d) Ag/AgBr ((a, b and d) scale bars = 1.00 μm; (c) scale bar = 3.00 μm). Reproduced with permission from ref. 152. Copyright 2018 Elsevier.

small mounds (Fig. 12-II). Due to the surface plasmon resonance of small-sized Ag nanoparticles with uniform distribution, Ag/AgX photocatalysts had excellent catalytic activity for the visible light-driven photodegradation of methyl orange and methylene blue pollutants.

In the study of Chen *et al.*, a two-step sonochemical approach was described to prepare core/satellite $Cd(OH)_2$/Ag nanorods (Fig. S7-I†).[153] Firstly, $Cd(OH)_2$ nanorods were yielded from cadmium chloride in a base medium by a single ultrasound-aided reaction, and then changed into highly crystalline CdO nanorods after a thermal annealing process; afterwards, the CdO nanorods in the presence of Ag precursor underwent a second ultrasonication producing a $Cd(OH)_2$/Ag core/satellite complex, where a phase transformation occurred from the cubic structure of CdO to the monoclinic crystalline structure of $Cd(OH)_2$ followed by Ag nanodots being deposited on the $Cd(OH)_2$ surface. Recently, they employed a surfactant-free sonochemical approach to synthesize unique Fe_2O_3/ZrO_2 nanostructures with nanocube morphology,[154] and then achieved Au nanodots decorated on the Fe_2O_3/ZrO_2 composites by a one-step sonochemical method (Fig. S7-II†). Apart from the conclusion that the Fe/Zr molar ratio played an important role in catalytic activity for the production of liquid fuel or organic chemicals from syngas (CO and H_2), the dopant Au nanodots also served as a promoter to contribute to the enhanced catalysis of Fe_2O_3/ZrO_2 nanocubes, wherein 2.5 wt% Au significantly increased the CO conversion ratio. However, higher Au concentration (*e.g.*, 5 wt%) in the catalyst would in turn cause a deactivation effect due to the aggregation and poisoning of particles.

Via promoting the diffusion of metal ions or particles, the physical/mechanical effects of ultrasound can participate in doping and/or modification processes creating hybrid metal/metal compounds. By ultrasound irradiation, Belova *et al.* produced Au nanoparticle-intercalated mesoporous TiO_2 structures with an enhanced photocatalysis from a slurry containing Au colloids and TiO_2 particles, while Xiong *et al.* made $Zn(OAc)_2$ and $Mg(OAc)_2$ into photoluminescence-tunable Mg^{2+}-doped ZnO nanoparticles without MgO phase.[155,156] Recently, Xu and coworkers described a simple and facile ionic liquid-assisted sonochemical method to synthesize hexagonal and tetragonal $LnPO_4:Eu^{3+}$ nanostructures (Ln = La, Gd, Y),[157] where the acceleration effect of ionic liquid combined with ultrasound irradiation led to a rapid reaction rate. Perhaps related to the period of the sonication process, the as-synthesized $LnPO_4:Eu^{3+}$ displayed four different morphologies: nanowires, nanorods, nanowire bundles, and nanoparticles. By a modified sonochemical method using aloe vera gel as a surfactant, Nagabhushana *et al.* carried out the synthesis of Eu^{3+}-doped Y_2O_3 nanophosphors.[158] The sonication period had an important effect on the morphology of Eu^{3+}-doped Y_2O_3. If the sonication period was very short, the structure of nanophosphors easily agglomerated, and when the sonication period was prolonged but less than 6 h, the structure gradually became uniformly spherical with the size slightly reducing, and the agglomerated structure occurred again after more than 6 h because uniform structures were again increasing.

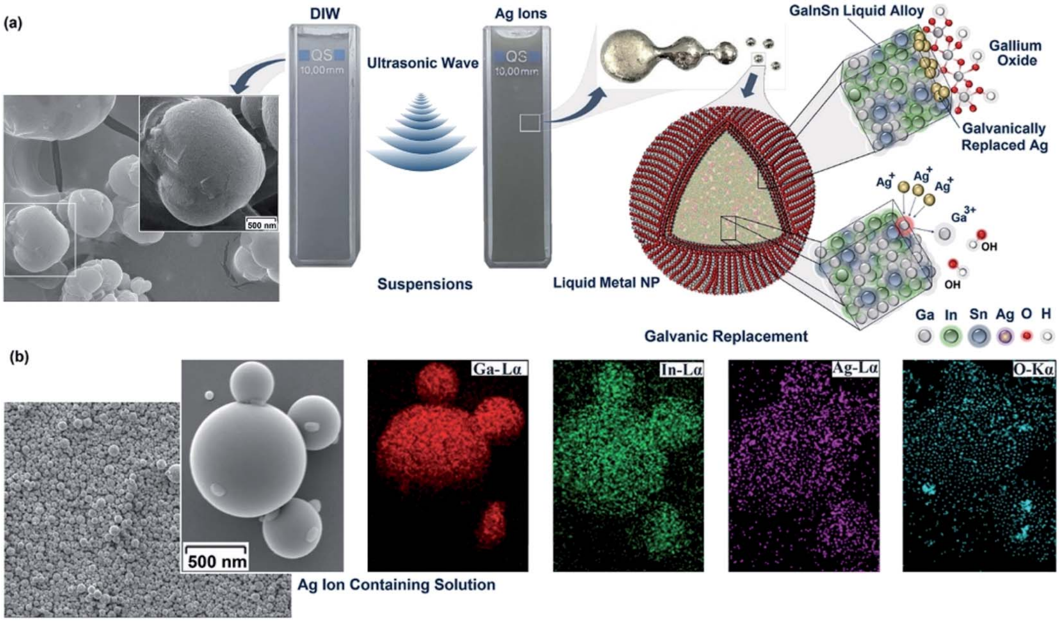

Fig. 13 (a) Schematic of ultrasonic-assisted synthesis of Galinstan nanoparticles in different ionic solutions. Left: formation of irregular shaped nanoparticles after ultrasonic-assisted synthesis of Galinstan nanoparticles (scale bar = 500 nm). The presence of fractured ultra-thin skin oxide on the nanoparticle surface is evidently seen. It seemed that during the size reduction of nanoparticles in the ultrasonic process, brittle skin oxides broke and separated from host liquid alloy. Right: schematic showing the sequential dispersion of liquid alloy under ultrasonic waves. The core–shell structure of Galinstan nanoparticles consists of a liquid InGaSn core covered with ultra-thin surface gallium oxide. (b) Spherical morphology (scale bar = 500 nm) of the nanoparticles and distribution of alloying elements on the surface of the nanoparticles synthesized in silver ion-containing solutions. Reproduced with permission from ref. 160. Copyright 2019 Royal Society of Chemistry.

With 1-butyl-3-methylimidazolium tetrafluoroborate as fluoride source and $EuBr_2$ or $EuSO_4$ as europium source, Wickleder *et al.* designed another novel ionic liquid-assisted strategy to fabricate Eu^{2+}-doped BaFCl nanoparticles by applying sonochemical approaches.[159] Such Eu^{2+}-doped nanoparticles in 1-butyl-3-methylimidazolium tetrafluoroborate presented a relatively narrow size distribution ranging from 20 to 90 nm with 80% being smaller than 40 nm. In the visible range, BaFCl nanoparticles doped with Eu^{2+} had a high reflectance value similar to that of undoped BaFCl nanoparticles owing to nearly no efficient absorption. In the UV spectral range, Eu^{2+}-doped BaFCl particles exhibited a decreased reflectance efficiently emitting bluish white light, even though the undoped particles also displayed weak dark blue emission probably attributed to the C-dot present in the ionic liquid. By the same synthesis route, $Ln(NO_3)_3$ and 1-hexyl-3-methylimidazoliumdihydric phosphate led to Eu^{3+}-doped lanthanide nanophosphates as well. Akbari *et al.* tried to use the functionalized surface oxide of liquid metals to build up advanced optoelectronic devices.[160] By employing the strong shear forces of ultrasound waves, liquid Galinstan could be simply fractured and separated in an aqueous solution, where ultra-thin Ga_2O_3 nanosheets could be achieved on the alloying nanoparticle surface with the nanoparticle core remaining liquid (Fig. 13). When Ag ions were present in the reacting system, the alloying nanoparticles acted as a sacrificial template where Ga with low standard reduction potential would be feasibly replaced by Ag ions with high standard reduction potential. The decoration of Ag facilitated the visible light responsivity of Ga_2O_3 nanosheets.

7.2. Metal/non-metal materials

There are many approaches to combine metals with non-metals forming hybrid materials, for example, doping, intercalation, coating, decoration, *etc.* Gedanken *et al.* produced carbon dots doped with Ga atoms (Ga@C-dots) when sonicating molten Ga and polyethylene glycol in a reaction medium for 30–120 min.[161] The Ga@C-dots were monodispersed and spherical in shape, and had an average size of about 5 nm with a range of 3 to 8 nm, while the pristine C-dots produced from polyethylene glycol had

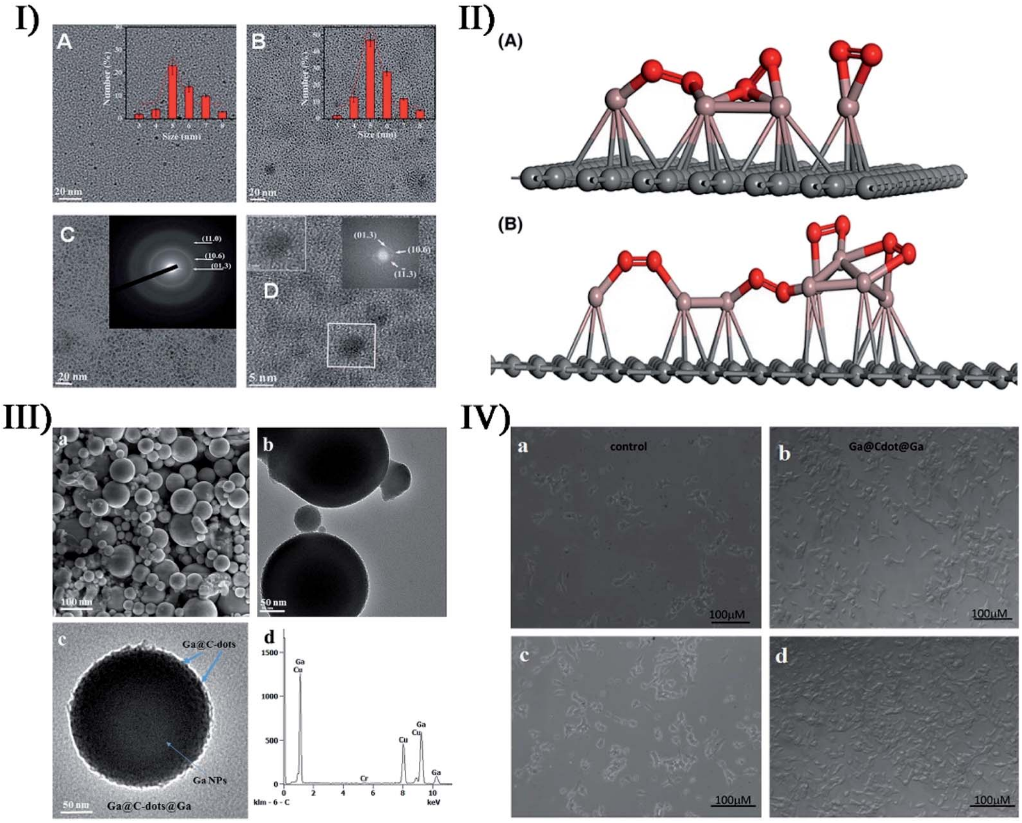

Fig. 14 (I) TEM images (scale bars = 20 nm) of C-dots: (A) PEG sonicated without gallium and (B) with gallium presented with a size distribution plot; (C) HRTEM image (scale bar = 20 nm) of Ga@C-dots synthesized by PEG in the presence of molten Ga (inset: SAED pattern marked by plane); (D) HRTEM images (scale bars = 5 nm) of Ga@C-dots (inset: lattice fringes of Ga@C-dots). Reproduced with permission from ref. 161. Copyright 2015 Royal Society of Chemistry. (II) Proposed structure for (A) Ga-dodecane sample and (B) Ga-decane sample from current characterization data (red: gallium, violet: oxygen, gray: carbon). Reproduced with permission from ref. 162. Copyright 2017 American Ceramic Society. (III) SEM micrograph ((a) scale bar = 100 nm), TEM image ((b) scale bar = 50 nm), magnified view ((c) scale bar = 50 nm) of single particles, and (d) EDS spectrum of Ga@C-dots@Ga nanoparticles. (IV) Light microscopy images for the growth rate of SH-SY5Y cells: cells growing on a glass substrate after (a) 2 days and (c) 7 days, and cells growing on the Ga@C-dots@Ga substrate after 2 days (b) and 7 days (d). Reproduced with permission from ref. 163. Copyright 2017 Royal Society of Chemistry.

an average size of about 6 nm (Fig. 14-I). The dopant Ga induced the crystallinity of C-dots and enhanced the formation of more C-dots with uniform size, so Ga@C-dots in selected area electron diffraction (SAED) revealed a ring pattern corresponding to a hexagonal carbon structure. With respect to C-dots, the Ga@C-dots had high photosensitization producing more singlet oxygen, which was significant for biomedical applications. Later, Kumar *et al.* investigated the interaction between molten gallium and the hydrocarbon medium induced by ultrasonic energy, so as to explore the possibility that the product was gallium carbide or another gallium–carbon complex.[162] When the sonication of molten gallium immersed in decane, dodecane and hexadecane was carried out, the partial decomposition of the hydrocarbon medium would occur and form a carbon film surrounding a gallium core prior to the interaction between carbon and gallium (Fig. 14-II). Thus, it was not a kinetic barrier but a thermodynamic barrier against the formation of gallium carbide. Based on the antibacterial activity of Ga@C-dots, Gedanken *et al.* further fabricated Ga@C-dots@Ga nanoparticles by Ga-doped C-dots decorated on Ga nanoparticles,[163] when 2.5 h of ultrasound irradiation with 70% amplitude caused the dispersion of molten Ga in the form of particles (Fig. 14-III). Once the Ga@C-dots@Ga nanoparticles were coated on the cell incubation substrate, the cell growth exhibited a 97% increase in the number of branches for the neurites deriving from the soma (Fig. 14-IV).

Ultrasound irradiation is a facile method to dramatically enhance the intercalation of guest substances into layered materials. In the study of Walter *et al.*,[164] H_2PtCl_6 was intercalated into natural graphite under ultrasound, and after exposure to a H_2 flow, Pt-intercalated graphite could be formed by the reduction of Pt ions to metal nanoparticles in the graphite layers. Jones and coworkers prepared K-intercalated compounds (KC_8) by sonicating graphite with potassium in toluene,[165] but the formation was difficult to achieve in either THF or hexane. This could be responded by the possibility that an aromatic solvent was necessary for interplanar expansion or intercalation prior to the addition of potassium to the lattice. In fact, the highly efficient exfoliation for graphene using sonication can also be carried out in the presence of inorganic ions (*e.g.*, SO_4^{2-}, NO_3^-, Cl^-, Li^+, Na^+, *etc.*), and has attracted much interest. Such successful exfoliation for few-layer nanosheets is often the result of ion intercalation with the aid of the physical effects of ultrasound irradiation. To realize the eco-friendly production of graphene, Cheng *et al.* designed an ultrasonic-assisted Li^+/Na^+ co-intercalated exfoliation route for few-layer graphene without organic solvent,[166] wherein mixed Li^+ and Na^+ served as the intercalated agent of natural flake graphite to prepare the as-exfoliated graphene before the exfoliation of graphene nanosheets. The variation of Li^+/Na^+ ratio affected the structure and morphology of graphene nanosheets, and the thicknesses of products were about 2.38–2.56 nm (about 7–8 layers) at the optimal Li^+/Na^+ ratio (namely $Li_{0.7}/Na_{0.3}$).

Coating or decoration is pervasive and efficient for the combination of heterogeneous materials. Lacroix-Desmazes *et al.* used a three-step process (*i.e.*, latex synthesis, sonochemistry, and sol–gel) to produce a silica-supported Pt catalyst in aqueous medium, and enhanced the distribution of noble metal Pt at low loadings by controlling the hierarchical porosity of silica material.[167] Zhang *et al.* prepared metal/non-metal hybrids by a ternary NiCoPd nanocatalyst dispersed on multi-walled carbon nanotubes (CNTs),[168] where the NiCo nanoparticles from Co^{2+} and Ni^{2+} were mixed with the CNT solution under ultrasonication followed by the reducing and loading of the third ion Pd^{2+} on the NiCo/CNTs in the presence of $NaBH_4$. The NiCoPd/CNT hybrids exhibited an enhanced electrocatalytic activity for the methanol oxidation reaction, which likely resulted from the synergistic function of doped Ni and Co metals as well as the size and distribution of ternary-metal nanoparticles. In the fabrication of platinum-based electrocatalysts, Okoli *et al.* developed carbon-supported palladium–nickel–molybdenum materials by a sonochemical method using ionic liquid as a dispersion medium.[169] After depositing a platinum monolayer on the ternary PdNiMo nanoparticle cores, the carbon-supported electrocatalysts could improve cathode activity and durability during the oxygen reduction reaction of a fuel cell.

Yang *et al.* reported, for the first time, a facile and powerful method to integrate hollow Pt–M (M = Ni, Co) nanoparticles into graphene cellular monoliths (GCMs) by using sonochemical-assisted reduction together with gelatinization reaction (Fig. S8-I†).[170] Firstly, the Pt^{2+} and M^{2+} precursors were ultrasonically reduced to three-dimensional hollow Pt–M nanoparticles in the presence of sodium borohydride and distributed on GO sheets. Then the transformation of GO into graphene was successfully achieved *via* an ascorbic acid reduction, and the as-synthesized Pt–M/graphene hybrid materials were assembled into Pt–M/GCM hydrogels. The Pt–M/GCM had a well-defined macroscopic porous structure on which hollow Pt–Ni or Pt–Co nanoparticles with a size of 10–17 nm were uniformly distributed (II and III in Fig. S8†).[170] Obviously, Pt–M nanoparticles promoted the formation of hierarchical porous structures and caused high specific surface areas and large total pore volumes. Compared with commercial Pt/C, the Pt–M/GCM had better electrocatalytic activity and higher durability toward oxygen reduction reaction. Abbas's group synthesized morphology-controlled Cu nanoparticles wrapped on reduced graphene oxide (Cu/RGO) when $Cu(NO_3)_2$ and GO as the precursor were subjected to an *in situ* ultrasonication reaction prior to the reduction of pre-product CuO/RGO in H_2 gas.[171] The morphology and catalytic performance of Cu/RGO were affected by ultrasound, NH_4OH, and Cu loading. For the pre-product CuO/RGO, the absence of NH_4OH resulted in polydisperse CuO particles with irregular shapes or amorphous-like structure, and without the aid of ultrasound, the produced Cu catalyst had an elongated-like shape with thick RGO layers owing to aggregation, whereas ultrasound alone was also not enough to completely reduce the GO into RGO. The Cu/RGO catalysts with a 10 wt% or 25 wt% Cu loading had an excellent dispersion and without any aggregation (Fig. S8-IV†),[171] but on the contrary, the morphology with a 45 wt% Cu loading appeared to be a leaf-like shape. In the catalytic hydrogenation reaction of dimethyl oxalate, Cu/RGO catalysts with 25 wt% Cu loading displayed the highest selectivity to methyl glycolate, while the catalysts with 45 wt% Cu loading favored the selectivity to ethanol.

7.3. Metal compounds/metal compounds

Among metal compounds, the all-out cooperation has attracted much attention for the preparation, properties and applications. In the study of Zavala-Rivera *et al.*,[172] iron carbide@iron oxide nanoparticles with core–shell architecture (around 6.38 nm in diameter) were obtained when the sonochemical reaction of $Fe(CO)_5$ in octanol was carried out under an inert air condition or pure oxygen condition. According to the composition of iron carbide core and magnetite shell, a supposed synthesis mechanism was described as follows. With the aid of oxygen, the decarbonization of $Fe(CO)_5$ produced the nucleation points of iron carbide (Fe_3C) due to the hotspot formation by cavitation. Afterwards, an iron oxide (γ-Fe_2O_3) layer (thickness of around 2.5 nm) was gradually formed *via* the secondary interaction of iron carbide and oxygen. Such iron carbide@iron oxide nanoparticles presented a ferromagnetic behavior at 4 K, suggesting a potential application in theranostics. Jiang *et al.* reported a facile two-step route to fabricate a ZnO/CdS hierarchical heterostructure (average size of approximately 2 μm) with enhanced photocatalytic efficiency under natural sunlight.[173] The hierarchical ZnO microspheres with ultrathin nanosheets (thickness of about 20 nm) as secondary structures were firstly synthesized through a hydrothermal method, following which hexagonal wurtzite CdS nanoparticles with diameters between 50 and 100 nm were produced by sonicating cadmium chloride and thiourea and then incorporated on the wurtzite ZnO sheets. Under natural sunlight, the ZnO/CdS heterostructures exhibited higher photocatalytic activity or degradation efficiency than pure ZnO sample, and the CdS loading amount was crucial for the photocatalytic performance, because the visible-light-absorbing capability of the hybrid material was enhanced by the coupling effects of the two semiconductors.

Adhyapak *et al.* attempted to merge hetero-valent tin oxide (Sn_3O_4) with ZnO, since ZnO with a wide band gap (3.2 eV) could be a good alternative for band coupling with Sn_3O_4 to fulfil the effective separation and transfer of photo-generated holes and electrons.[174] By a combined hydrothermal and sonochemical method, they synthesized a ZnO@Sn_3O_4 nano-heterostructure composite, where a nanosheet-like Sn_3O_4 structure with a thickness of 20 nm was decorated with hexagonal rod-like ZnO of 50–180 nm in width and 200–400 nm in length (Fig. 15-I). Compared to pristine ZnO and Sn_3O_4, ZnO@Sn_3O_4 showed a significantly superior photocatalytic activity towards dye

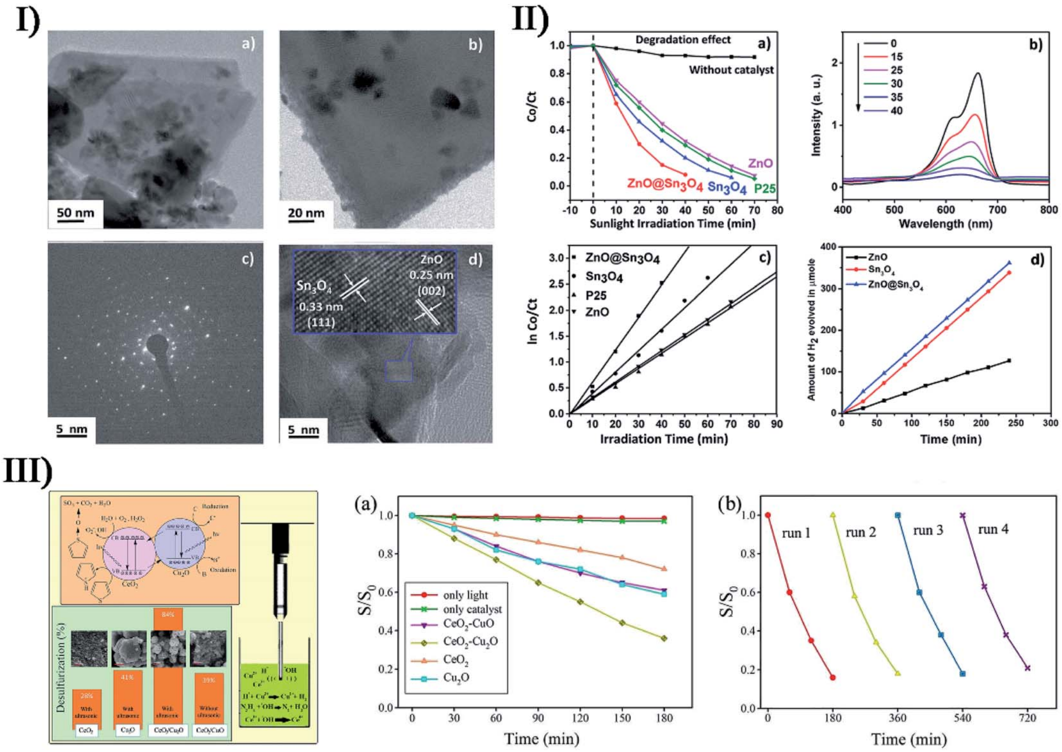

Fig. 15 (I) TEM images ((a) scale bar = 50 nm; (b) scale bar = 20 nm), SAED pattern image ((c) scale bar = 5 nm), and HRTEM image ((d) scale bar = 5 nm) of ZnO@Sn_3O_4. (II) (a) Plot of change in absorbance *vs.* irradiation time in the presence of ZnO, Sn_3O_4, P25 and ZnO@Sn_3O_4, (b) spectral changes for the degradation of methylene blue in the presence of ZnO@Sn_3O_4, (c) pseudo-first-order kinetic plots of $\ln(C_0/C_t)$ *vs.* irradiation time for the degradation of methylene blue using ZnO, Sn_3O_4, P25 and ZnO@Sn_3O_4, and (d) hydrogen production as a function of irradiation time in the presence of ZnO, Sn_3O_4 and ZnO@Sn_3O_4. Reproduced with permission from ref. 174. Copyright 2019 Royal Society of Chemistry. (III) Schematic mechanism for the photocatalytic oxidation of thiophene on Cu_2O–CeO_2 nanocomposite: (a) photocatalytic oxidation of thiophene under visible light irradiation by CuO–CeO_2, Cu_2O–CeO_2, CeO_2 and Cu_2O, and (b) repeatability of as-synthesized Cu_2O–CeO_2 nanocomposite. Reproduced with permission from ref. 175. Copyright 2020 Elsevier.

degradation as well as hydrogen production *via* water splitting, and the complete degradation of methylene blue was achieved within 40 min under natural sunlight (Fig. 15-II).[174] Aiming at thiophene photocatalytic oxidative desulfurization, Mousavi-Kamazani and coworkers utilized a facile and single-step sonochemical method to prepare composite Cu_2O–CeO_2 nanostructures from $Ce(NO_3)_3$ and $Cu(NO_3)_2$ (Fig. 15-III).[175] Interestingly in the absence of ultrasound irradiation, the main product was not Cu_2O–CeO_2 but CuO–CeO_2, implying that ultrasound irradiation facilitated the reduction of Cu^{2+} to Cu^+. Besides the composition, ultrasound irradiation had a direct effect on the product morphology, and Cu_2O–CeO_2 composite nanoparticles were smaller in size (about 10 nm) and higher in uniformity unlike agglomerated CuO–CeO_2 structures. Compared with CuO–CeO_2, Cu_2O–CeO_2 exhibited much higher photocatalytic efficiency for thiophene oxidative desulfurization under visible light because hexagonal-like Cu_2O nanostructures in the heterostructure not only increased the amount of light absorption but also had an electron-synergistic effect to promote electron–hole separation.

TiO_2 is a known semiconductor material in light science, and has an excellent photocatalytic activity under UV light. Nevertheless, the separation of photoinduced electron–hole pairs restricts the photocatalysis of TiO_2. Therefore, combining TiO_2 with other transition metal semiconductors is a usual and efficient approach to overcome this issue. By sonochemical catalysis with a 480 W ultrasound irradiation of 40 kHz, Majumder *et al.* fabricated crystalline hexagonal disk-shaped anatase TiO_2 within manganese oxide (Mn_2O_3) nanorods forming TiO_2–Mn_2O_3 composites.[176] The synthesized TiO_2–Mn_2O_3 had unique morphology including nanorods and nanodisks, which could provide higher surface area to enhance the adsorption efficiency and promote the electron–hole separation. In comparison to the composites obtained by a sol–gel method, TiO_2–Mn_2O_3 showed a comparable photocatalytic decolorization efficiency when the decomposition of malachite green oxalate was carried out under ultraviolet irradiation, and with an aid of ultrasound-functionalized H_2O_2, the photoactivity of such a catalyst was found to be higher than that of all bare samples. To extend the absorption of TiO_2 to the visible region, Fallah *et al.* employed an ultrasonic method in combination with microemulsion to prepare core–shell CdS/TiO_2 nanoparticles (*i.e.*, CdS core and TiO_2 shell) and control their particle size.[177] By optimizing the influential parameters such as temperature, synthesis retention time, TiO_2/CdS ratio and ultrasound power, nanocomposites with an average size of up to 10 nm were successfully synthesized, namely a nano-sized TiO_2 layer (about 1 nm) fully enclosed the CdS core (about 9 nm), as shown in Fig. S9.†[177] Owing to the participation of CdS in the core–shell composites, the absorption spectra of TiO_2 occurred with a red shift, suggesting the optical absorption spectrum of nanocrystals had extended to the visible region.

In the report from Cheng *et al.*,[178] TiO_2@ZIF-8 composite materials made up of hollow TiO_2 nanospheres (TiO_2 HNPs) and zeolitic imidazolate framework-8 (ZIF-8) were fabricated *via* a facile sonochemical or sonocrystallization route. Spherical polystyrene with a uniform size was selected as the template in the preparation of polystyrene@TiO_2 core–shell particles, and after annealing to remove the polystyrene, the obtained TiO_2 hollow nanospheres (shell thickness of 60 nm) were carboxylated and externally decorated with ZIF-8 that was produced by a self-nucleus growth under ultrasonic treatment, forming double-shell γ-TiO_2@ZIF-8 hybrid materials (Fig. 16-II).[178] *Via* experimental sequences different from the overall

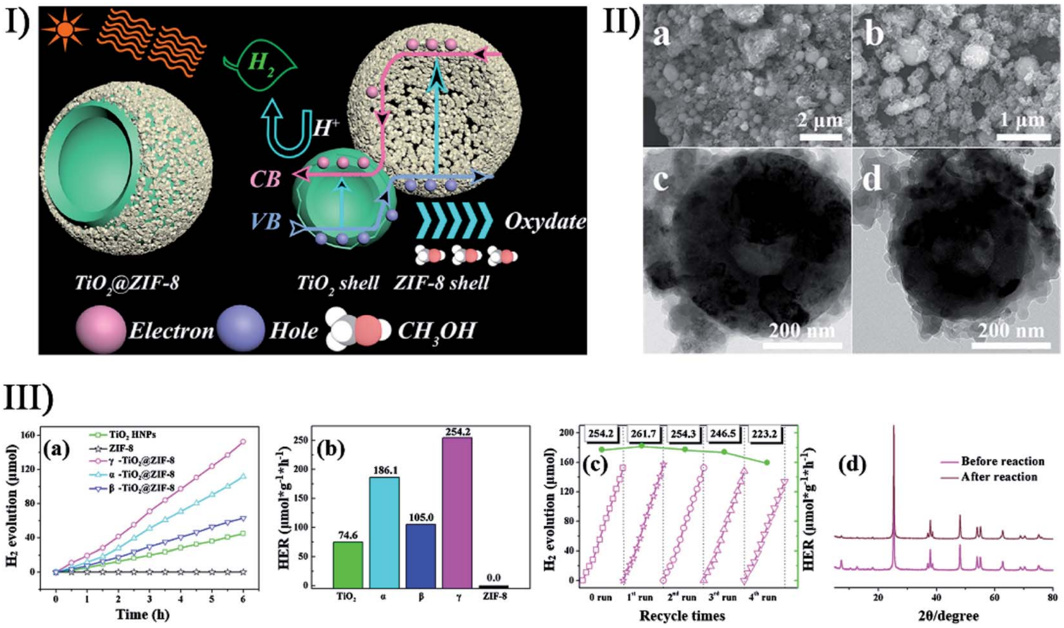

Fig. 16 (I) Illustration of hydrogen evolution mechanism over TiO_2@ZIF-8 under artificial solar light irradiation. (II) SEM images ((a) scale bar = 2 μm; (b) scale bar = 1 μm) and TEM images ((c and d) scale bar = 200 nm) of γ-TiO_2@ZIF-8. (III) (a) Photocatalytic hydrogen evolution performance of TiO_2 HNPs, ZIF-8 and α-/β-/γ-TiO_2@ZIF-8, (b) H_2 evolution rates, (c) recyclability of H_2 evolution behavior of γ-TiO_2@ZIF-8, and (d) PXRD patterns of γ-TiO_2@ZIF-8 before and after recycling 4 times. Reproduced with permission from ref. 178. Copyright 2019 Elsevier.

sonocrystallization, two other kinds of semiconductor–metal organic framework samples were also produced, namely α- and β-TiO_2@ZIF-8, whereas some failures occurred in ZIF-8 coverage on the surface of TiO_2 HNPs due to the over-independence of two components. The large surface area and high porosity of hollow TiO_2 and ZIF-8 would expose more active sites in photocatalysis, and the composite heterostructures provided efficient charge separation with electron injection from ZIF-8 to hollow TiO_2 (Fig. 16-I).[178] Under artificial solar light, the hybrid double-shell γ-TiO_2@ZIF-8 exhibited an enhanced hydrogen evolution rate, 3.5 times higher than that of the bare TiO_2 HNPs, with up to 50.89% apparent quantum efficiency at 380 nm (Fig. 16-III). Moreover, the hydrogen evolution rate remained nearly the same after several consecutive photocatalytic reactions, demonstrating the exceptional photocatalytic stability of γ-TiO_2@ZIF-8.[178]

7.4. Metal compounds/non-metal materials

The coupling of metal compounds and non-metal materials catches the eye as a consequence of their superior complementation in particular domains. Carbon materials are popularly selected for many composites not only for their incomparable chemical, physical and/or mechanical properties but also for their variety in structure. Nikitenko *et al.* carried out the sonolysis of $W(CO)_6$ in diphenylmethane under 20 kHz power ultrasound in argon at 80 °C,[179] and the pre-product WC_x nanoparticles were embedded in amorphous sonopolymer followed by carbon-supported WC_x nanoparticles (W_2C/C) being created after annealing in an inert atmosphere at 600 °C. The W_2C/C nanocomposites were stable and consisted of amorphous W_2C with average particle size ranging from 4 to 7 nm and hexagonal carbon particles with average size of 30–40 nm. Later, Yamada *et al.* prepared an amorphous iron/carbon mixture by the sonolysis of ferrocene in diphenylmethane.[180] Interestingly, the Fe and C atoms migrated to consistently form a spherical Fe–C phase with diameters of about 50 nm when the pre-produced amorphous sample was subjected to heating at 900 °C, but the product would be accompanied by carbon nanotubes if heated at 1200 °C, which was caused by the catalysis of iron or iron carbide nanoparticles. In order to

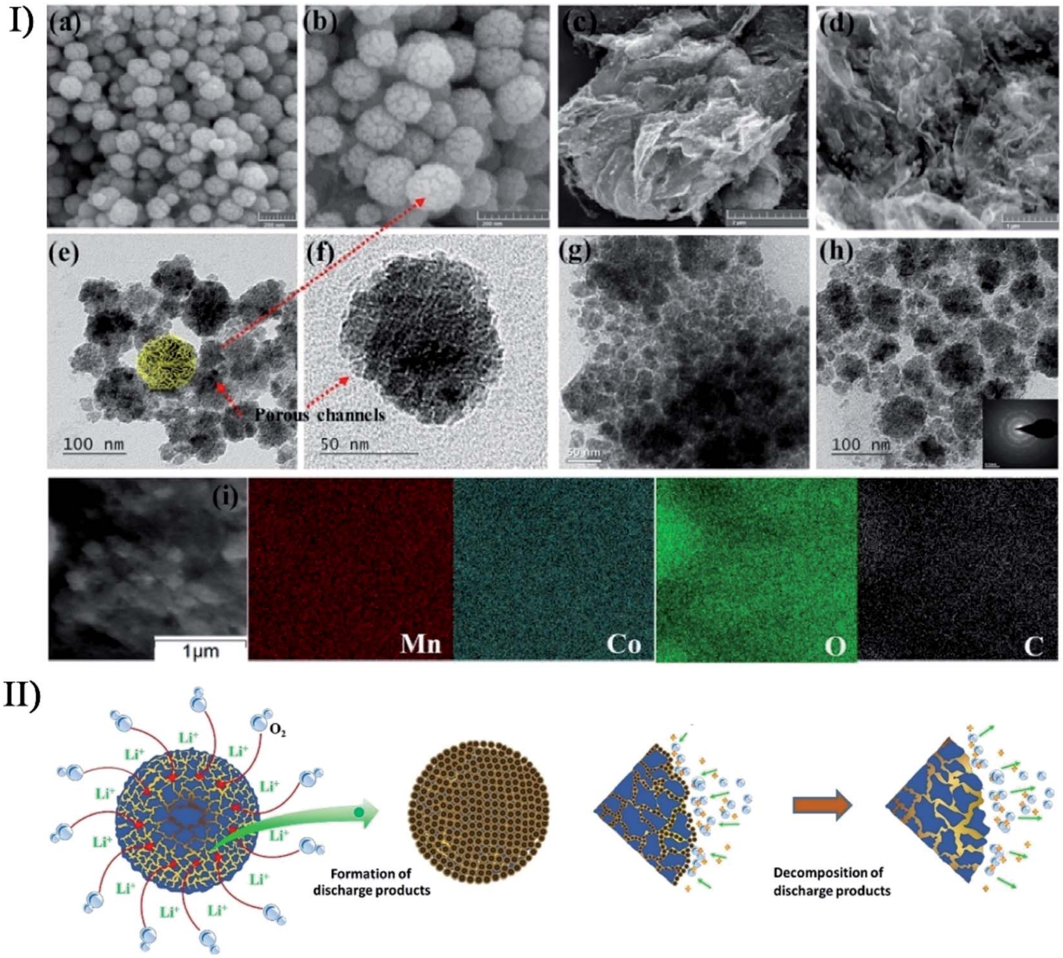

Fig. 17 (I) Microscopic images of $MnCo_2O_4$: FESEM images of $MnCo_2O_4$ ((a and b) scale bar = 200 nm) and $MnCo_2O_4$/graphene composite ((c) scale bar = 2 μm; (d) scale bar = 1 μm); TEM images of $MnCo_2O_4$ ((e) scale bar = 100 nm; (f) scale bar = 50 nm) and $MnCo_2O_4$/graphene composite ((g) scale bar = 50 nm; (h) scale bar = 100 nm), as well as SAED pattern (inset); (i) EDX mapping images of Mn, Co, O, and C elements. (II) Schematic representation of the formation-decomposition mechanism of discharged products on $MnCo_2O_4$/graphene hybrid cathodes. Reproduced with permission from ref. 183. Copyright 2017 Wiley.

develop an efficient and durable catalyst for the oxygen evolution reaction, Xu *et al.* reported the synthesis of amorphous nickel-iron oxides/carbon nanohybrids (a-NiFeO$_x$/C) with tunable compositions *via* a sonochemical method.[181] As an electrocatalyst, the compositions of mixed-metal oxides conveniently affected the activities of the oxygen evolution reaction, wherein the optimal a-Ni$_{50}$Fe$_{50}$O$_x$/C exhibited a low overpotential, outperforming the benchmark RuO$_2$ catalyst. Sonochemistry, as another assisting factor, provided the nickel-iron oxides/carbon nanohybrids with highly stable amorphism remaining even after prolonged cycling, and led to a simultaneously formed carbon scaffold and internal Ni(0), which was important to enhance the stability and activity for the oxygen evolution reaction.

Metal compound-based composites with graphene or GO as a support are diverse and abundant. Zhu *et al.* succeeded in a controlled incorporation of TiO$_2$ nanoparticles on graphene layers homogeneously by ultrasonically irradiating graphene and TiCl$_4$ in ethanol.[182] In terms of photocatalytic activity, the graphene–TiO$_2$ composite containing 25 wt% TiO$_2$ was better than commercial pure TiO$_2$. This was due to the graphene–TiO$_2$ composite structure consisting of a homogeneous dispersion of crystalline TiO$_2$ nanoparticles with extremely small size (around 4–5 nm) on the graphene sheets, and the good contact between the two materials enhanced the photo-electron conversion of TiO$_2$ through reducing the recombination of photo-generated electron–hole pairs. Prakash *et al.* reported the sonochemical synthesis of nanoporous MnCo$_2$O$_4$/graphene as a hybrid cathode material in non-aqueous Li–O$_2$ batteries (Fig. 17-I).[183] The product offered a strong synergistic coupling between MnCo$_2$O$_4$ nanospheres and graphene sheets, and a porous nanosphere architecture with internal oxygen diffusion pathways and peripheral conductive graphene sheet extensions fulfilled the requirements of a robust cathode and overcame the harsh LiO$_2$ battery conditions (Fig. 17-II),[183] so when catalyzing oxygen reduction, MnCo$_2$O$_4$/graphene exhibited better rate capability than the widely used Vulcan carbon and benchmark Pt/C catalysts, as well as excellent cycling stability and low overpotential. Zhang *et al.* sonochemically synthesized SnO$_2$/graphene nanocomposites from SnCl$_2$ and GO precursors,[184] and SnO$_2$ nanoparticles were *in situ* created, and fully and well adhered on the two sides of graphene nanosheets by the reduction of GO under continuous ultrasonication after Sn^{2+} was homogeneously dispersed on the GO surface. The resulting SnO$_2$/graphene structure had high specific surface area, a stable framework, and remarkable electron/ion transport, and hence, compared to bare SnO$_2$, the SnO$_2$/graphene nanocomposites serving as a lithium ion battery anode exhibited significantly improved specific capacity, better cycling stability, and competitive rate performance. In the study of Chen *et al.*,[185] (ZrO$_2$-Al$_2$O$_3$)/GO nanocomposites with special 3D network were successfully prepared by a sonochemical catalysis route, where the coexisting Zr and Al sources quickly produced metal oxide nanoparticles aggregated on the GO surface under ultrasound irradiation. Owing to a good fluoride adsorption capacity, the nanocomposites exhibited exceptionally high defluoridation performance for drinking water. Similarly, ZnO is also often deposited on carbon materials using ultrasound-assisted approaches. For example, Cobianu *et al.* prepared 3D nanostructured ZnO–graphene hybrids for gas sensing applications, while Khairy *et al.* employed an ultrasonic/hydrothermal process to fabricate ZnO nanosphere-carbon nanotube nanocomposites and ZnO nanosphere-rGO nanocomposites for the heterogeneous photocatalytic degradation of 4-nitrophenol.[186,187]

So far, many efforts have been also made to prepare metal compound/silica materials. Santoyo-Salazar *et al.* obtained core–shell Fe$_3$O$_4$@SiO$_2$ *via* the combination of Stöber and sonochemical methods using low-power ultrasound irradiation, where magnetite nanoparticles were coated with silica.[188] With an increase of tetraethyl orthosilicate volume, the composites had a controlled SiO$_2$ layer encapsulating crystalline Fe$_3$O$_4$ distribution. In order to validate the mechanism of sonoluminescence in SiO$_2$ suspensions, Sharipov *et al.* produced porous SiO$_2$ nanoparticles containing Ru$_3$(CO)$_{12}$ with a size range of 10–30 nm and an average pore size of 5.8 nm *via* ultrasonic dispersal,[189] ahead of which the pores on the precursor micro-mesoporous silica powder (particle size of 100–300 μm, and average pore size of 5.8 nm) were saturated with ruthenium dodecacarbonyl by solvent evaporation. In some studies, metal compound-based SiO$_2$ composites have been developed to form nanocatalysts. Kim *et al.* employed a short-time sonochemical method for the synthesis of PdO-doped silica nanocomposites,[190] in which PdO nanoparticles were deposited on the silica surface without aggregation. Compared with unsupported PdO nanoparticles, the PdO-doped composites had higher catalytic activity and selectivity for the aerobic alcohol oxidation reaction due to the synergetic effect of PdO with the silica support. In the presence of a basic agent, Salavati-Niasari *et al.* fabricated Nd$_2$O$_3$–SiO$_2$ nanocomposites using ultrasonic waves for decomposition.[191] By adjusting the mole ratio of Si and Nd, type of basic agent and ultrasonic power, Nd$_2$O$_3$–SiO$_2$ nanocomposites were optimized in terms of shape, size and photocatalytic activity. Under ultraviolet illumination, the decomposition efficiency of the as-formed nanocatalyst toward methyl violet contaminant was remarkably increased, suggesting the introduction of SiO$_2$ to Nd$_2$O$_3$ had an important effect on the catalytic performance of Nd$_2$O$_3$.

Also, other metal compound/inorganic materials have been developed for on-demand applications. Akbari *et al.* reported the decoration of Se nanostructure on the surface of Ga$_2$O$_3$ nanosheets to facilitate the visible light responsivity of Ga$_2$O$_3$, which was similar to the proposal that they modulated the surface properties of Ga$_2$O$_3$ nanosheets with Ag nanostructure.[160] Chen *et al.* fabricated CuFe$_2$O$_4$/g-C$_3$N$_4$ composite nanostructures by a two-step sonochemical route at a frequency of 20 kHz and power of 70 W,[192] where sphere-like CuFe$_2$O$_4$ nanoparticles were synthesized using sonochemical and hydrothermal techniques in basic medium and then fixed on graphitic carbon nitride (g-C$_3$N$_4$) nanosheets by a second ultrasonication producing network-like magnetic nanocomposites (Fig. 18-I). Such CuFe$_2$O$_4$/g-C$_3$N$_4$ exhibited better electrochemical activity towards the oxidation of xanthine to uric acid with higher anodic current, larger linear range and lower detection limit (Fig. 18-II).[192] Nowee and coworkers utilized ultrasound-assisted precipitation to synthesize Cu(OH)$_2$/g-C$_3$N$_4$ photocatalysts for hydrogen production from

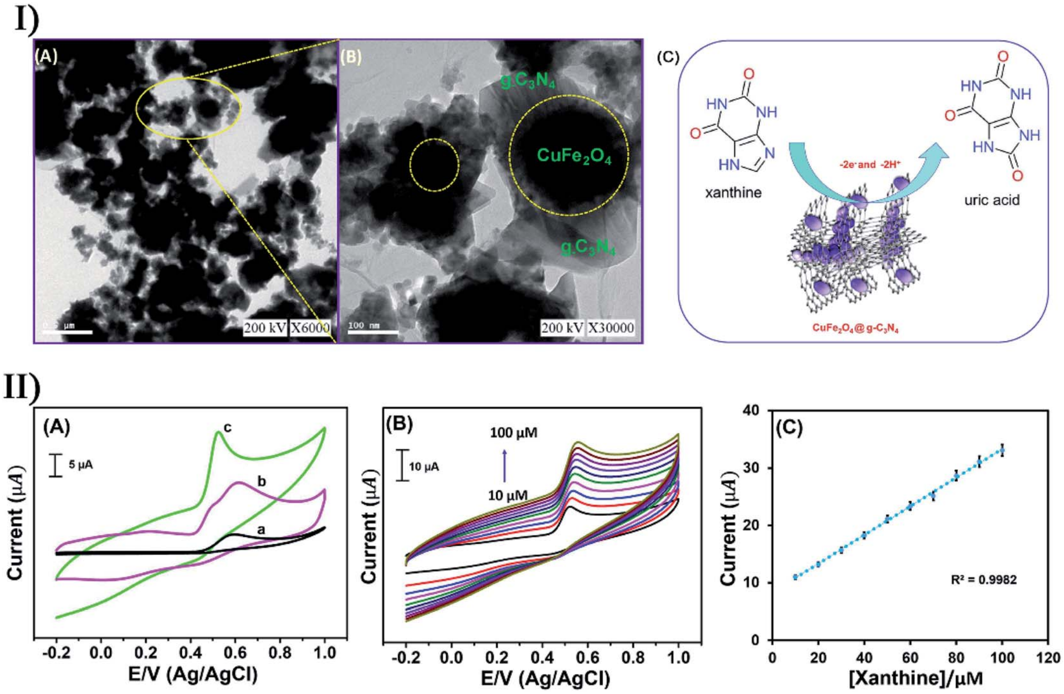

Fig. 18 (I) TEM analysis of $CuFe_2O_4$/g-C_3N_4 ((A) scale bar = 0.5 μm; (B) scale bar = 100 nm), and electrochemical oxidation mechanism of xanthine based on $CuFe_2O_4$/g-C_3N_4/SPCE (C). (II) (A) Electrochemical oxidation of xanthine using (a) bare SPCE, (b) g-C_3N_4/SPCE and (c) $CuFe_2O_4$/g-C_3N_4/SPCE; (B) electrochemical detection of xanthine with different concentrations (10–100 μM); (C) anodic current *vs.* different concentrations. Reproduced with permission from ref. 192. Copyright 2020 Elsevier.

water splitting under visible light.[193] The product demonstrated a higher performance (about 31 times) than pure C_3N_4 because the stable $Cu(OH)_2$ cocatalyst acted as electron traps and active sites. Certainly, ultrasound irradiation provided an intimate cocatalyst-semiconductor interfacial contact, higher surface area and better dispersion of cocatalysts, which facilitated the efficient transfer of electrons to cocatalyst and decreased the recombination of charge carriers. In the study of Lv *et al.*,[194] g-C_3N_4 loaded with MoS_x nanodots (3–20 nm) was successfully prepared by ultrasonic treatment. MoS_x/g-C_3N_4 had better photocatalytic H_2 evolution performance than Pt/g-C_3N_4, but its activity decreased with time probably ascribed to the photocorrosion of MoS_x. To overcome this, Ni was deposited on the surface of MoS_x nanodots by *in situ* photo-deposition, producing more stable Ni–MoS_x/g-C_3N_4 cocatalysts under visible light. The resultant composites inhibited the recombination of electron–hole pairs excited in g-C_3N_4 and provided more active sites for hydrogen evolution, causing a much better photocatalytic performance.

7.5. Other composites

There are numerous and varied inorganic composites that do not belong to the defining categories in the above description. For instance, Badhulika *et al.* prepared red-black phosphorus from low-cost red phosphorus *via* a simple scalable sonication process,[195] and then combined the hybrid phosphorus with sulfonated porous carbon in an ultrasound-assisted carbonization process, yielding red-black phosphorus/sulfonated porous carbon composites. The synergistic combination of red-black phosphorus and sulfonated porous carbon provided shorter pathways for the ion diffusion and rapid electron transfer, and the composites exhibited a high structural stability attributed to the carbon network with phosphorus bonding and heteroatom doping. Hence the red-black phosphorus/sulfonated porous carbon was able to serve as a high-performance supercapacitor electrode to deliver superior capacitive properties towards energy storage devices. To improve the efficiency of dye-sensitized solar cells, Salavati-Niasari *et al.* prepared two kinds of GQDs/Sb_2S_3/TiO_2 ternary hybrids using an ultrasonic probe with 60 W cm^{-2} intensity and 18 kHz frequency.[196] When analyzing the electronic structure of GQDs/Sb_2S_3/TiO_2, the nanomaterials with Sb_2S_3 inserted between GQDs and TiO_2 were more stable than those with Sb_2S_3 placed on GQDs/TiO_2. The band gap of GQDs/Sb_2S_3/TiO_2 was less than that of TiO_2 and GQDs/TiO_2 so that the electronic transition from the valence band to the conduction band was easier and the photocatalytic performance was stronger. In the reports of Mortazavi-Derazkola *et al.* and Orooji *et al.*,[197,198] sonochemical synthesis produced nanocomposite-based platforms for drug delivery and photocatalytic degradation, respectively. Wherein, mesoporous Fe_3O_4@SiO_2–hydroxyapatite showed low toxicity, high drug loading, slow release and biodegradation,[197] while Fe_3O_4/SiO_2/ZnO–Pr_6O_{11} nanocomposites displayed remarkably enhanced photocatalytic activity towards rhodamine B and Congo red degradation under UV irradiation.[198]

Hybrid structures simultaneously consisting of metal, metal compounds and nonmetal compounds have been emerging in large numbers in the field of sonochemical synthesis. Kipp *et al.* developed an ultrasound-assisted technique to create *in situ* gold nanocrystals on the surface of silica-coated CdSe-dot/CdS-rod core/shell nanoparticles (Fig. 19-I),[199] where polyethylene glycol acted as the solvent and reducing agent for Au^{3+} ions. Due to the high viscosity of polyethylene glycol, the mobility of gold precursors was efficiently decreased to prevent the penetration of Au^{3+} into the silica shell whose surface promoted the heterogeneous nucleation of Au nanocrystals. Besides, the collective effect from polyethylene glycol and ultrasound irradiation ensured the formation of Au nanocrystals with a relatively narrow size distribution ranging from 2 to 7 nm (Fig. 19-II).[199] With the aid of the hybrid structures, the strong plasmon-exciton interaction between the CdSe-dot/CdS-rod and Au nanocrystals decreased the photoluminescence decay rate and suppressed fluorescence blinking behavior. Wang *et al.* reported the fabrication of magnetic-based flower-like silver microflowers through a sonochemistry-assisted strategy,[200] where the product was comprised of a 200 nm Fe_3O_4 core, a 50 nm SiO_2 inner shell and a highly branched Ag petal outer shell (Fig. 19-III). The size and morphology of Ag petals on the Fe_3O_4@SiO_2@Ag microflowers could be well controlled and tuned by varying the concentrations of Ag precursor. Owing to the large effective surface area of the branched Ag petals, Fe_3O_4@SiO_2@Ag microflowers were capable of forming sufficient plasmonic hotspots and capturing target molecules. The Fe_3O_4 core with good magnetic responsiveness allowed enrichment of the targeted analytes and creation of abundant interparticle hotspots *via* magnetism-induced aggregation, and made the versatile microflowers easily recycled or reproducible as a surface-enhanced Raman scattering substrate. As for non-adsorbed R6G molecules or adsorbed pesticide thiram, Fe_3O_4@SiO_2@Ag had corresponding detection limits as low as 1×10^{-14} M or 1×10^{-11} M (Fig. 19-IV),[200] and it could easily capture *S. aureus* in tap water when functionalized by aptamers, and significantly enhanced the surface-enhanced Raman scattering signal. Fe_3O_4/SiO_2/Pr, graphene–Ce–TiO_2 and graphene–Fe–TiO_2 nanocomposites also have been fabricated in the

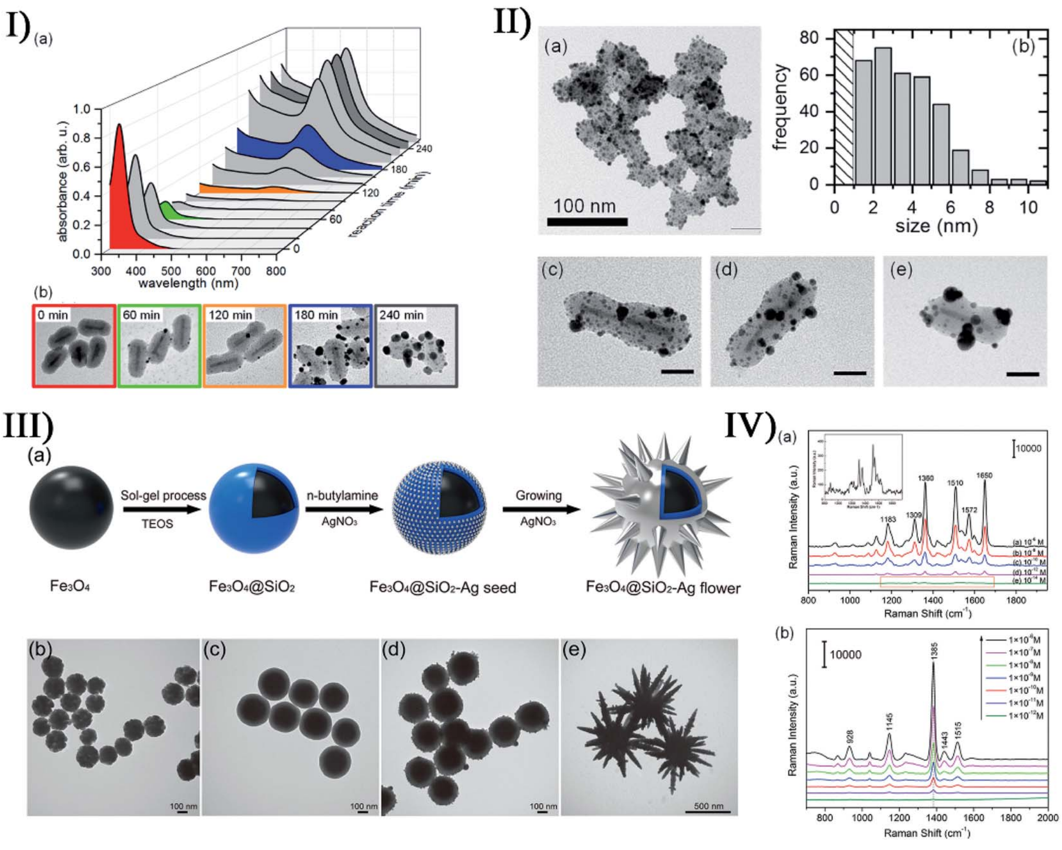

Fig. 19 (I) (a) Evolution of the absorption spectra of CdSe-dot/CdS-rod/SiO_2-$HAuCl_4$-PEG mixture under ultrasound irradiation as a function of the reaction time, and (b) TEM images of the samples after different reaction times, where the frame color of each image (50 nm × 50 nm in scale) corresponds to that of the absorbance plot as displayed in (a). (II) TEM image ((a) scale bar = 100 nm) of an aggregation of CdSe-dot/CdS-rod/SiO_2-Au hybrid nanoparticles after 4 h reaction time, (b) corresponding Au particle size distribution histogram, and TEM images ((c–e) scale bars = 20 nm) of individual CdSe-dot/CdS-rod/SiO_2-Au hybrid nanoparticles. Reproduced with permission from ref. 199. Copyright 2019 American Chemical Society. (III) Schematic of the synthetic process of Fe_3O_4@SiO_2@Ag microflowers (a), and TEM images (scale bars = 100 nm) of (b) Fe_3O_4, (c) Fe_3O_4@SiO_2, (d) Fe_3O_4@SiO_2-Ag seed and (e) Fe_3O_4@SiO_2@Ag microflowers. (IV) Surface-enhanced Raman scattering spectra of (a) R6G and (b) thiram at different concentrations on the Fe_3O_4@SiO_2@Ag microflowers, where the inset shows a magnified view of spectrum E in (a). Reproduced with permission from ref. 200. Copyright 2016 Royal Society of Chemistry.

presence of ultrasound irradiation, with the aim of being employed for the photocatalytic degradation of organic dyes.[201,202]

Furthermore, rare earth ions often participate in the sonochemical synthesis of inorganic composites. Muniswamy *et al.* reported excellent assembly of $BaTiO_3:Eu^{3+}@SiO_2$ superstructures using CTAB as a surfactant.[203] The nanocomposites had a broomlike structure because CTAB kinetically controlled the growth rates of various faces by interacting with the faces through adsorption and desorption when chemically adsorbed onto the surface of nucleated $BaTiO_3:Eu^{3+}$ nanoparticles. Thus, the CTAB concentration was an influential parameter to set in favor of nucleation and growth of crystals. Certainly, the pH of reactants and ultrasound irradiation time were also involved in the growth mechanism of the broomlike architectures leading to core–shell entities. Compared to commercially available toxic dusting powders, dormant fingerprints could be visualized by $BaTiO_3:Eu^{3+}@SiO_2$ (5 mol%) as an efficient phosphor exhibiting high efficiency and high sensitivity. In the study of Kokila *et al.*, SiO_2-coated $SrTiO_3:Dy^{3+}$ (5 mol%) nanopowders were obtained on the basis of a low-temperature sonochemical route in the presence of bio-surfactant aloe vera gel extract. As compared to uncoated $SrTiO_3:Dy^{3+}$ (5 mol%),[204] $SiO_2@SrTiO_3:Dy^{3+}$ exhibited an increasing enhancement in the photoluminescence intensity with the numbers of SiO_2 coating layers probably owing to the passivation of surface states and the reduced surface defects of $SrTiO_3:Dy^{3+}$. As a labelling agent for the visualization of latent fingerprints and dosimetry, $SiO_2@SrTiO_3:Dy^{3+}$ exhibited high clarity, high sensitivity, low fading (20%), and good reproducibility (up to four cycles).

8. Future outlook of sonochemical catalysis in synthesis

Sonochemical catalysis has been developed for the synthesis of numerous materials owing to the simplicity and effectiveness of ultrasound irradiation. Ultrasound irradiation is also a useful tool to catalyze the reactions among other synthesis methods, where the shear force and intense shock waves allow a faster mass transfer to cause a better contact of reactants. Furthermore, ultrasonic treatment is usually able to increase the catalytic activity by changing the crystallinity of product materials, giving catalytic enhancement for reactions such as reduction, oxidation, degradation, polymerization, and so on.[205]

In the future, there are still some probable challenges to overcome in both the design of ultrasound-assisted approaches and the controllability of product properties. For instance, the indeterminacy of sonochemical catalysis may bring two-sidedness to the synthesis platforms as a result of the deficient mechanistic and experimental understanding of the cavitation phenomenon; sonochemical catalysis should have a chance to assemble pre-defined materials for purpose-specific or site-specific modification; the synergy of ultrasound irradiation with other synthesis methods or technologies should be highly demanding to control morphologies, structures, sizes and compositions; the resultant nano/micro devices still have to emphasize the activity, stability, durability, selectivity, low cost, long shelf life, or other requirements; and regarding the synthesis of inorganic materials *via* sonochemical catalysis, further studies also need to involve more mechanisms and product varieties for in-depth development. Certainly, sonochemical catalysis at the nano- and microscale levels will be explored according to on-site conditions or stimuli.

9. Conclusion

Ultrasound can act as a nonclassical mechanical method to directly or indirectly induce or strengthen some chemical syntheses. In this review, the basic principles of acoustic cavitation have been overviewed as well as the chemical effects and physical and/or mechanical effects from acoustic cavitation, which are responsible for sonochemical catalysis. According to the latest developments, sonochemical catalysis has been described with emphasis on the synthesis of nano/micro inorganic structures including metals, metal compounds, nonmetal materials, and inorganic composites, and many aspects are covered in detail with morphologies, structures, sizes, properties and applications of well-designed products. Also, the review points out the prospective challenges and trends in ultrasound-assisted synthesis, highlighting the significance of sonochemical catalysis. The ultrasound-assisted methods or sonochemical catalysis are versatile in material preparation or modification as a unique strategy, and will be an available future direction to broaden applications in catalysis, biomedicine or other fields.

Conflicts of interest

The authors declare no conflict of interest.

Acknowledgements

The authors would like to thank Natural Science Foundation of Shandong (2018GGX102030), Taishan Scholar Program of Shandong Province (ts201511027), China Postdoctoral Science Foundation (2017M622125), and Research Project of Postdoctoral Application in Qingdao. The authors thank Royal Society of Chemistry, Elsevier, American Chemical Society, Springer and Wiley-VCH for copyright permissions of reproduction, adaptation, and redrawing of figures.

Notes and references

1 B. M. Teo, Ultrasonic synthesis of polymer nanoparticles, *Handbook of Ultrasonics and Sonochemistry*, 2015, pp. 1–29.
2 L. H. Thompson and L. K. Doraiswamy, Sonochemistry: science and engineering, *Ind. Eng. Chem. Res.*, 1999, **38**, 1215–1249.
3 K. Yamamoto, P. M. King, X. Wu, T. J. Mason and E. M. Joyce, Effect of ultrasonic frequency and power on the disruption of algal cells, *Ultrason. Sonochem.*, 2015, **24**, 165–171.

4 J. Gonzalez-Garcia, V. Saez, I. Tudela, M. I. Diez-Garcia, M. D. Esclapez and O. Louisnard, Sonochemical treatment of water polluted by chlorinated organocompounds. A review, *Water*, 2010, **2**, 28–74.

5 M. Siddique, R. Farooq, Z. M. Khan, Z. Khan and S. Shaukat, Enhanced decomposition of reactive blue 19 dye in ultrasound assisted electrochemical reactor, *Ultrason. Sonochem.*, 2011, **18**, 190–196.

6 M. Bradley, M. Ashokkumar and F. Grieser, Sonochemical production of fluorescent and phosphorescent latex particles, *J. Am. Chem. Soc.*, 2003, **125**, 525–529.

7 M. T. Taghizadeh and T. Asadpour, Effect of molecular weight on the ultrasonic degradation of poly(vinylpyrrolidone), *Ultrason. Sonochem.*, 2009, **16**, 280–286.

8 J. P. Canselier, H. Delmas, A. M. Wilhelm and B. Abismail, Ultrasound emulsification-an overview, *J. Dispersion Sci. Technol.*, 2002, **23**, 333–349.

9 N. K. Morya, P. K. Iyer and V. S. Moholkar, A physical insight into sonochemical emulsion polymerization with cavitation bubble dynamics, *Polymer*, 2008, **49**, 1910–1925.

10 X. Du, Z. Li, J. Xia, F. Zhang and Z. Wang, Facile sonochemistry-assisted assembly of the water-loving drug-loaded micro-organogel with thermo- and redox-sensitive behavior, *Colloids Surf., A*, 2019, **561**, 47–56.

11 Z. Li, X. Du, X. Cui and Z. Wang, Ultrasonic-assisted fabrication and release kinetics of two model redoxresponsive magnetic microcapsules for hydrophobic drug delivery, *Ultrason. Sonochem.*, 2019, **57**, 223–232.

12 D. Rodriguezsanmiguel, C. Montoro and F. Zamora, Covalent organic framework nanosheets: preparation, properties and applications, *Chem. Soc. Rev.*, 2020, **49**, 2291–2302.

13 M. Huo, L. Wang, Y. Chen and J. Shi, Nanomaterials/microorganism-integrated microbiotic nanomedicine, *Nano Today*, 2020, 100854.

14 G. Chatel, How sonochemistry contributes to green chemistry?, *Ultrason. Sonochem.*, 2018, **40**, 117–122.

15 T. J. Mason, Industrial, sonochemistry: potential and practicality, *Ultrasonics*, 1992, **30**, 192–196.

16 N. Pokhrel, P. K. Vabbina and N. Pala, Sonochemistry: science and engineering, *Ultrason. Sonochem.*, 2016, **29**, 104–128.

17 E. K. Skinner, *Sonochemical production of hollow polymer microspheres for responsive delivery*, University of Bath, 2013.

18 N. K. Draye, Advances in green organic sonochemistry, *Top. Curr. Chem.*, 2016, **374**, 74.

19 K. Hanajiri, T. Maruyama, Y. Kaneko, H. Mitsui, S. Watanabe, M. Sata, R. Nagai, T. Kashima, J. Shibahara, M. Omata and Y. Matsumoto, Microbubble-induced increase in ablation of liver tumors by high-intensity focused ultrasound, *Hepatol. Res.*, 2006, **36**, 308–314.

20 Y. S. Tung, H. L. Liu, C. C. Wu, K. C. Ju, W. S. Chen and W. L. Lin, Contrast-agent-enhanced ultrasound thermal ablation, *Ultrasound Med. Biol.*, 2006, **32**, 1103–1110.

21 C. Zhou, F. Li, Y. Qin, C. Liu, X. Zheng and Z. Wang, Non-thermal ablation of rabbit liver VX2 tumor by pulsed high intensity focused ultrasound with ultrasound contrast agent: pathological characteristics, *World J. Gastroenterol.*, 2008, **14**, 6743–6747.

22 D. G. Shchukin and H. Moehwald, Sonochemical nanosynthesis at the engineered interface of a cavitation microbubble, *Phys. Chem. Chem. Phys.*, 2006, **8**, 3496–3506.

23 A. Tinoco, A. Ribeiro, C. Oliveira, P. Parpot, A. Gomes and A. Cavaco-Paulo, Albumin/asparaginase capsules prepared by ultrasound to retain ammonia, *Appl. Microbiol. Biotechnol.*, 2016, **100**, 9499–9508.

24 Z. Li, Z. Wang, X. Du, C. Shi and X. Cui, Sonochemistry-assembled stimuli-responsive polymer microcapsules for drug delivery, *Adv. Healthcare Mater.*, 2018, **7**, 1701326.

25 M. Vinatoru and T. J. Mason, Can sonochemistry take place in the absence of cavitation?—a complementary view of how ultrasound can interact with materials, *Ultrason. Sonochem.*, 2019, **52**, 2–5.

26 Y. Zhang, Y. Gao and X. Du, Stability mechanisms of oscillating vapor bubbles in acoustic fields, *Ultrason. Sonochem.*, 2018, **40**, 808–814.

27 C. R. Brenner, *Cavitation and bubble dynamics*, Oxford University Press, Oxford, 1995.

28 K. S. Suslick, N. C. Eddingsaas, D. J. Flannigan, S. D. Hopkins and H. X. Xu, The chemical history of a bubble, *Acc. Chem. Res.*, 2018, **51**, 2169–2178.

29 T. G. McKenzie, F. Karimi, M. Ashokkumar and P. G. G. Qiao, Ultrasound and sonochemistry for radical polymerization: sound synthesis, *Chem.–Eur. J.*, 2019, **25**, 5372–5388.

30 R. Silva, H. Ferreira, N. G. Azoia, U. Shimanovich, G. Freddi, A. Gedanken and A. C. Paulo, Insights on the mechanism of formation of protein microspheres in a biphasic system, *Mol. Pharmaceutics*, 2012, **9**, 3079–3088.

31 R. Ji, R. Pflieger, M. Virot and S. I. Nikitenko, Multibubble sonochemistry and sonoluminescence at 100 kHz: the missing link between low- and high-frequency ultrasound, *J. Phys. Chem. B*, 2018, **122**, 6989–6994.

32 J. J. Hinman and K. S. Suslick, Nanostructured materials synthesis using ultrasound, *Sonochemistry*, 2017, 59–94.

33 K. S. Suslick, Sonochemistry, *Science*, 1990, **247**, 1439–1445.

34 J. R. Blake and D. C. Gibson, Cavitation bubbles near boundaries, *Annu. Rev. Fluid. Mech.*, 1987, **19**, 99–123.

35 C. D. Ohl, T. Kurz, R. Geisler, O. Lindau and W. Lauterborn, Bubble dynamics, shock waves and sonoluminescence, *Philos. Trans. R. Soc., London, Ser. A*, 1999, **357**, 269.

36 D. G. Shchukin, D. Radziuk and H. Moehwald, Ultrasonic fabrication of metallic nanomaterials and nanoalloys, *Annu. Rev. Mater. Res.*, 2010, **40**, 345–362.

37 J. H. Bang and K. S. Suslick, Applications of ultrasound to the synthesis of nanostructured materials, *Adv. Mater.*, 2010, **22**, 1039–1059.

38 Z. Li, X. Du, X. Cui and Z. Wang, Ultrasonic-assisted fabrication and release kinetics of two model redoxresponsive magnetic microcapsules for hydrophobic drug delivery, *Ultrason. Sonochem.*, 2019, **57**, 223–232.

39 M. A. Bhosale, D. R. Chenna and B. M. Bhanage, One-step sonochemical irradiation dependent shape controlled crystal growth study of gold nano/microplates with high

catalytic activity in degradation of dyes, *ChemistrySelect*, 2016, **3**, 504–512.

40 K. S. Suslick, S. B. Choe, A. A. Cichowlas and M. W. Grinstaff, Sonochemical synthesis of amorphous iron, *Nature*, 1991, **353**, 414–416.

41 K. S. Suslick, M. Fang and T. Hyeon, Sonochemical synthesis of iron colloids, *J. Am. Chem. Soc.*, 1996, **118**, 11960–11961.

42 N. Enomoto, S. Hirata, M. Inada and K. Hayashi, Crystallization behavior of iron-based amorphous nanoparticles prepared sonochemically, *Ultrason. Sonochem.*, 2017, **35**, 563–568.

43 M. W. Grinstaff, A. A. Cichowlas, S. B. Choe and K. S. Suslick, Effect of cavitation conditions on amorphous metal synthesis, *Ultrasonics*, 1992, **30**, 168–172.

44 Y. Koltypin, G. Katabi, X. Cao, R. Prozorov and A. Gedanken, Sonochemical preparation of amorphous nickel, *J. Non-Cryst. Solids*, 1996, **201**, 159–162.

45 D. G. Shchukin, E. Skorb, V. Belova and H. Moehwald, Ultrasonic cavitation at solid surfaces, *Adv. Mater.*, 2011, **23**, 1922–1934.

46 K. Okitsu, M. Ashokkumar and F. Grieser, Sonochemical synthesis of gold nanoparticles: effects of ultrasound frequency, *J. Phys. Chem. B*, 2005, **109**, 20673–20675.

47 K. Yasuda, T. Sato and Y. Asakura, Size-controlled synthesis of gold nanoparticles by ultrafine bubbles and pulsed ultrasound, *Chem. Eng. Sci.*, 2020, **217**, 115527.

48 K. Okitsu, K. Sharyo and R. Nishimura, One-pot synthesis of gold nanorods by ultrasound irradiation: the effect of pH on the shape of the gold nanorods and nanoparticles, *Langmuir*, 2009, **25**, 7786–7790.

49 A. Sánchez-Iglesias, I. Pastoriza-Santos, J. Pérez-Juste, B. Rodríguez-González, F. J. García de Abajo and L. M. Liz-Marzán, Synthesis and optical properties of gold nanodecahedra with size control, *Adv. Mater.*, 2006, **18**, 2529–2534.

50 N. S. M. Yusof and M. Ashokkumar, Sonochemical synthesis of gold nanoparticles by using high intensity focused ultrasound, *ChemPhysChem*, 2015, **16**, 775–781.

51 H. Xu and K. S. Suslick, Sonochemical synthesis of highly fluorescent Ag nanoclusters, *ACS Nano*, 2010, **4**, 3209–3214.

52 T. Liu, L. Zhang, H. Song, Z. Wang and Y. Lv, Sonochemical synthesis of Ag nanoclusters: electrogenerated chemiluminescence determination of dopamine, *Luminescence*, 2013, **28**, 530–535.

53 T. Zhou, M. Rong, Z. Cai, C. J. Yang and X. Chen, Sonochemical synthesis of highly fluorescent glutathione-stabilized Ag nanoclusters and S^{2-} sensing, *Nanoscale*, 2012, **4**, 4103–4106.

54 J. Li, C. J. Ke, C. Lin, Z. H. Cai, C. Y. Chen and W. H. Chang, Facile method for gold nanocluster synthesis and fluorescence control using toluene and ultrasound, *J. Med. Biol. Eng.*, 2013, **33**, 23–28.

55 C. Wang, H. Cheng, Y. Huang, Z. Xu, H. Lin and C. Zhang, Facile sonochemical synthesis of pH-responsive copper nanoclusters for selective and sensitive detection of Pb^{2+} in living cells, *Analyst*, 2015, **140**, 5634–5639.

56 Y. Jia, T. Sun, Y. Jiang, W. Sun, Y. Zhao, J. Xin, Y. Hou and W. Yang, Green, fast, and large-scale synthesis of highly fluorescent Au nanoclusters for Cu^{2+} detection and temperature sensing, *Analyst*, 2018, **143**, 5145–5150.

57 M. Kamali, M. Davarazar and T. M. Aminabhavi, Single precursor sonochemical synthesis of mesoporous hexagonal-shape zero-valent copper for effective nitrate reduction, *Chem. Eng. J.*, 2020, **384**, 123359.

58 C. Gümeci, Z. R. Li, D. J. Casadonte and J. C. Korzeniewski, Pt-Ni nanoparticles for oxygen reduction prepared by a sonochemical method, *J. Electrochem. Soc.*, 2012, **159**, F35–F41.

59 C. Gumeci, D. U. Cearnaigh, D. J. Casadonte and J. C. Korzeniewski, Synthesis of $PtCu_3$ bimetallic nanoparticles as oxygen reduction catalysts via a sonochemical method, *J. Mater. Chem. A*, 2013, **1**, 2322–2330.

60 H. Ataee-Esfahani, L. Wang, Y. Nemoto and Y. Yamauchi, Synthesis of bimetallic Au@Pt nanoparticles with Au core and nanostructured Pt shell toward highly active electrocatalysts, *Chem. Mater.*, 2010, **22**, 6310–6318.

61 V. K. Harika, H. K. Sadhanala, I. Perelshtein and A. Gedanken, Sonication-assisted synthesis of bimetallic Hg/Pd alloy nanoparticles for catalytic reduction of nitrophenol and its derivatives, *Ultrason. Sonochem.*, 2020, **60**, 104804.

62 V. K. Harika, V. B. Kumar and A. Gedanken, One-pot sonochemical synthesis of Hg-Ag alloy microspheres from liquid mercury, *Ultrason. Sonochem.*, 2018, **40**, 157–165.

63 M. A. Matin, J. H. Jang and Y. U. Kwon, PdM nanoparticles (M = Ni, Co, Fe, Mn) with high activity and stability in formic acid oxidation synthesized by sonochemical reactions, *J. Power Sources*, 2014, **262**, 356–363.

64 M. A. Matin, J. H. Jang and Y. U. Kwon, One-pot sonication-assisted polyol synthesis of trimetallic coreeshell (Pd,Co) @Pt nanoparticles for enhanced electrocatalysis, *Int. J. Hydrogen Energy*, 2014, **39**, 3710–3718.

65 Y. Mizukoshi, T. Fujimoto, Y. Nagata, R. Oshima and Y. Maeda, Characterization and catalytic activity of core-shell structured gold/palladium bimetallic nano vparticles synthesized by the sonochemical method, *J. Phys. Chem. B*, 2000, **104**, 6028–6032.

66 S. Anandan, F. Grieser and M. Ashokkumar, Sonochemical synthesis of Au-Ag core-shell bimetallic nanoparticles, *J. Phys. Chem. C*, 2008, **112**, 15102–15105.

67 A. Godínez-García, J. F. Pérez-Robles, H. V. Martínez-Tejada and O. Solorza-Feria, Characterization and electrocatalytic properties of sonochemical synthesized PdAg nanoparticles, *Mater. Chem. Phys.*, 2012, **134**, 1013–1019.

68 M. N. Alam, S. Das, S. Batuta, D. Mandal and N. A. Begum, Green-nanochemistry for safe environment: bio-friendly synthesis of fluorescent monometallic (Ag and Au) and bimetallic (Ag/Au alloy) nanoparticles having pesticide sensing activity, *J. Nanostruct. Chem.*, 2016, **6**, 373–395.

69 T. Hyeon, M. Fang and K. S. Suslick, Nanostructured molybdenum carbide: sonochemical synthesis and catalytic properties, *J. Am. Chem. Soc.*, 1996, **118**, 5492–5493.

70 Y. Koltypin, X. Cao, R. Prozorov, J. Balogh, D. Kaptas and A. Gedanken, Sonochemical synthesis of iron nitride nanoparticles, *J. Mater. Chem.*, 1997, **7**, 2453–2456.

71 P. M. Sakkas, C. Bozes, D. G. Kanellopoulou, G. Sourkouni and C. Argirusis, A study on the synchronous decoration of molybdenum oxide or tungsten oxide nanoparticles on anode materials for natural gas fed solid oxide fuel cells using ultrasounds, *Ultrason. Sonochem.*, 2019, **59**, 104715.

72 J. Stubbings, J. Brown and G. J. Price, Sonochemical production of nanoparticle metal oxides for potential use in dentistry, *Ultrason. Sonochem.*, 2017, **35**, 646–654.

73 M. Gancheva, M. Markova-Velichkova, G. Atanasova, D. Kovacheva, I. Uzunov and R. Cukeva, Design and photocatalytic activity of nanosized zinc oxides, *Appl. Surf. Sci.*, 2016, **368**, 258–266.

74 M. A. Almessiere, Y. Slimani, H. Güngüneş, V. G. Kostishyn, S. V. Trukhanov, A. V. Trukhanov and A. Baykal, Impact of Eu^{3+} ion substitution on structural, magnetic and microwave traits of Ni-Cu-Zn spinel ferrites, *Ceram. Int.*, 2020, **46**, 11124–11131.

75 B. Ünal, M. A. Almessiere, A. D. Korkmaz, Y. Slimani and A. Baykal, Effect of thulium substitution on conductivity and dielectric belongings of nanospinel cobalt ferrite, *J. Rare Earths*, 2020, **38**, 1103–1113.

76 A. Sadaqat, M. Almessiere, Y. Slimani, S. Guner, M. Sertkol, H. Albetran, A. Baykal, S. E. Shirsath, B. Ozcelik and I. Ercan, Structural, optical and magnetic properties of Tb^{3+} substituted Co nanoferrites prepared via sonochemical approach, *Ceram. Int.*, 2019, **45**, 22538–22546.

77 S. Rehman, M. A. Almessiere, F. A. Khan, A. D. Korkmaz, N. Tashkandi, Y. Slimani and A. Baykal, Synthesis and biological characterization of $Mn_{0.5}Zn_{0.5}Eu_xDy_xFe_{1.8-2x}O_4$ nanoparticles by sonochemical approach, *Mater. Sci. Eng., C*, 2020, **109**, 110534.

78 M. A. Almessiere, Y. Slimani, A. V. Trukhanov, A. D. Korkmaz, S. Guner, S. Akhtar, S. E. Shirsath, A. Baykal and I. Ercan, Effect of Nd-Y co-substitution on structural, magnetic, optical and microwave properties of NiCuZn nanospinel ferrites, *J. Mater. Res. Technol.*, 2020, **9**, 11278–11290.

79 M. A. Almessiere, Y. Slimani, M. Sertkol, F. A. Khan, M. Nawaz, H. Tombuloglu, E. A. Al-Suhaimi and A. Baykal, Ce-Nd Co-substituted nanospinel cobalt ferrites: an investigation of their structural, magnetic, optical, and apoptotic properties, *Ceram. Int.*, 2019, **45**, 16147–16156.

80 M. A. Almessiere, A. V. Trukhanov, F. A. Khan, Y. Slimani, N. Tashkandi, V. A. Turchenko, T. I. Zubar, D. I. Tishkevich, S. V. Trukhanov, L. V. Panina and A. Baykal, Correlation between microstructure parameters and anti-cancer activity of the $[Mn_{0.5}Zn_{0.5}](Eu_xNd_xFe_{2-2x})O_4$ nanoferrites produced by modified sol-gel and ultrasonic methods, *Ceram. Int.*, 2020, **46**, 7346–7354.

81 M. A. Almessiere, Y. Slimani, S. E. Shirsath, Y. S. Wudil, A. Baykal and I. Ercan, Customized magnetic properties of $(Mn_{0.5}Zn_{0.5})[Eu_xNd_xFe_{2-2x}]O_4$ nanospinel ferrites synthesized via ultrasonic irradiation approach, *Results Phys.*, 2020, **19**, 103350.

82 M. A. Almessiere, B. Ünal, Y. Slimani, A. D. Korkmaz, A. Baykal and I. Ercan, Electrical properties of La^{3+} and Y^{3+} ions substituted $Ni_{0.3}Cu_{0.3}Zn_{0.4}Fe_2O_4$ nanospinel ferrites, *Results Phys.*, 2019, **15**, 102755.

83 M. A. Almessiere, Y. Slimani, A. D. Korkmaz, A. Baykal, H. Gungunes, H. Sozeri, S. E. Shirsath, S. Guner, S. Akhtar and A. Manikandan, Impact of La^{3+} and Y^{3+} ion substitutions on structural, magnetic and microwave properties of $Ni_{0.3}Cu_{0.3}Zn_{0.4}Fe_2O_4$ nanospinel ferrites synthesized via sonochemical route, *RSC Adv.*, 2019, **9**, 30671–30684.

84 Y. Slimani, B. Unal, M. A. Almessiere, A. D. Korkmaz, S. E. Shirsath, G. Yasin, A. V. Trukhanov and A. Baykal, Investigation of structural and physical properties of Eu^{3+} ions substituted $Ni_{0.4}Cu_{0.2}Zn_{0.4}Fe_2O_4$ spinel ferrite nanoparticles prepared via sonochemical approach, *Results Phys.*, 2020, **17**, 103061.

85 M. A. Almessiere, Y. Slimani, B. Unal, T. I. Zubar, A. Sadaqat, A. V. Trukhanov and A. Baykal, Microstructure, dielectric and microwave features of $[Ni_{0.4}Cu_{0.2}Zn_{0.4}](Fe_{2-x}Tb_x)O_4$ $(x \leq 0.1)$ nanospinel ferrites, *J. Mater. Res. Technol.*, 2020, **9**, 10608–10623.

86 Y. Slimani, M. A. Almessiere, A. D. Korkmaz, S. Guner, H. Güngüneş, M. Sertkol, A. Manikandan, A. Yildiz, S. Akhtar, S. E. Shirsath and A. Baykal, $Ni_{0.4}Cu_{0.2}Zn_{0.4}Tb_xFe_{2-x}O_4$ nanospinel ferrites: ultrasonic synthesis and physical properties, *Ultrason. Sonochem.*, 2019, **59**, 104757.

87 M. A. Almessiere, Y. Slimani, S. Guner, M. Sertkol, A. D. Korkmaz, S. E. Shirsath and A. Baykal, Sonochemical synthesis and physical properties of $Co_{0.3}Ni_{0.5}Mn_{0.2}Eu_xFe_{2-x}O_4$ nano-spinel ferrites, *Ultrason. Sonochem.*, 2019, **58**, 104654.

88 M. A. Almessiere, Y. Slimani, A. D. Korkmaz, S. Güner, A. Baykal, S. E. Shirsath, I. Ercan and P. Kögerler, Sonochemical synthesis of Dy^{3+} substituted $Mn_{0.5}Zn_{0.5}Fe_{2-x}O_4$ nanoparticles: structural, magnetic and optical characterizations, *Ultrason. Sonochem.*, 2020, **61**, 104836.

89 M. A. Almessiere, Y. Slimani, A. D. Korkmaz, N. Taskhandi, M. Sertkol, A. Baykal, S. E. Shirsath, I. Ercan and B. Ozçelik, Sonochemical synthesis of Eu^{3+} substituted $CoFe_2O_4$ nanoparticles and their structural, optical and magnetic properties, *Ultrason. Sonochem.*, 2019, **58**, 104621.

90 M. A. Almessiere, Y. Slimani, U. Kurtan, S. Guner, M. Sertkol, S. E. Shirsath, S. Akhtar, A. Baykal and I. Ercan, Structural, magnetic, optical properties and cation distribution of nanosized $Co_{0.7}Zn_{0.3}Tm_xFe_{2-x}O_4$ $(0.0 \leq x \leq 0.04)$ spinel ferrites synthesized by ultrasonic irradiation, *Ultrason. Sonochem.*, 2019, **58**, 104638.

91 M. A. Almessiere, Y. Slimani, A. D. Korkmaz, S. Guner, M. Sertkol, S. E. Shirsath and A. Baykal, Structural, optical and magnetic properties of Tm^{3+} substituted cobalt spinel ferrites synthesized via sonochemical approach, *Ultrason. Sonochem.*, 2019, **54**, 1–10.

92 Y. Slimani, M. A. Almessiere, M. Sertkol, S. E. Shirsath, A. Baykal, M. Nawaz, S. Akhtar, B. Ozcelik and I. Ercan, Structural, magnetic, optical properties and cation distribution of nanosized $Ni_{0.3}Cu_{0.3}Zn_{0.4}Tm_xFe_{2-x}O_4$ ($0.0 \le x \le 0.10$) spinel ferrites synthesized by ultrasound irradiation, *Ultrason. Sonochem.*, 2019, **57**, 203–211.

93 M. A. Almessiere, Y. Slimani, S. Rehman, F. A. Khan, E. G. Polat, A. Sadaqat, S. E. Shirsath and A. Baykal, Synthesis of Dy-Y co-substituted manganese-zinc spinel nanoferrites induced anti-bacterial and anti-cancer activities: comparison between sonochemical and sol-gel auto-combustion methods, *Mater. Sci. Eng., C*, 2020, **116**, 111186.

94 Y. Slimani, M. A. Almessiere, S. Guner, F. S. Alahmari, G. Yasin, A. V. Trukhanov and A. Baykal, Influence of Tm–Tb substitution on magnetic and optical properties of Ba-Sr hexaferrites prepared by ultrasonic assisted citrate sol-gel approach, *Mater. Chem. Phys.*, 2020, **253**, 123324.

95 M. A. Almessiere, Y. Slimani, H. Güngüneş, A. D. Korkmaz, A. Baykal, A. V. Trukhanov and G. Yasin, $SrCo_xZr_xFe_{12-2x}O_{19}$ and $SrNi_xZr_xFe_{12-2x}O_{19}$ hexaferrites: a Comparison Study of AC Susceptibility, FC-ZFC and hyperfine interactions, *Chin. J. Phys.*, 2020, **66**, 596–605.

96 M. A. Almessiere, Y. Slimani, S. Guner, S. Aldakhil, A. D. Korkmaz, M. Sertkol, H. Gungunes, G. Yasin and A. Baykal, Ultrasonic synthesis, magnetic and optical characterization of Tm^{3+} and Tb^{3+} ions co-doped barium nanohexaferrites, *J. Solid State Chem.*, 2020, **286**, 121310.

97 M. A. Almessiere, Y. Slimani, A. D. Korkmaz, A. Baykal, H. Albetran, T. A. Saleh, M. Sertkol and I. Ercan, A study on the spectral, microstructural, and magnetic properties of Eu-Nd double-substituted $Ba_{0.5}Sr_{0.5}Fe_{12}O_{19}$ hexaferrites synthesized by an ultrasonic-assisted approach, *Ultrason. Sonochem.*, 2020, **62**, 104847.

98 Y. Slimani, M. A. Almessiere, S. Güner, U. Kurtan and A. Baykal, Impacts of sol-gel auto-combustion and ultrasonication approaches on structural, magnetic, and optical properties of Sm-Tm co-substituted $Sr_{0.5}Ba_{0.5}Fe_{12}O_{19}$ nanohexaferrites: comparative study, *Nanomaterials*, 2020, **10**, 272.

99 M. M. Mdleleni, T. Hyeon and K. S. Suslick, Sonochemical synthesis of nanostructured molybdenum sulfide, *J. Am. Chem. Soc.*, 1998, **120**, 6189–6190.

100 R. Karthik, J. V. Kumar, S. Chen, P. Sundaresan, B. Mutharani, Y. C. Chen and V. Muthuraj, Simple sonochemical synthesis of novel grass-like vanadium disulfide: a viable non-enzymatic electrochemical sensor for the detection of hydrogen peroxide, *Ultrason. Sonochem.*, 2018, **48**, 473–481.

101 T. T. T. Le, T. V. Vu, H. Kim, D. Jeong, B. Pejjai, N. T. N. Truong and C. Park, Green and low-cost synthesis of CIGSe nanoparticles using ethanol as a solvent by a sonochemical method-A new approach, *Mater. Chem. Phys.*, 2018, **207**, 522–529.

102 S. Ramaraj, M. Sakthivel, S. Chen and K. Ho, Ultrasound-assisted synthesis of two-dimensional layered ytterbium substituted molybdenum diselenide nanosheets with excellent electrocatalytic activity for the electrochemical detection of diphenylamine anti-scald agent in fruit extract, *Ultrason. Sonochem.*, 2019, **50**, 265–277.

103 M. Yildirim, A. S. Kipcak and E. M. Derun, Sonochemical-assisted magnesium borate synthesis from different boron sources, *Pol. J. Chem. Technol.*, 2017, **19**, 81–88.

104 I. Doroshenko, J. Zurkova, Z. Moravec, P. Bezdicka and J. Pinkas, Sonochemical precipitation of amorphous uranium phosphates from trialkyl phosphate solutions and their thermal conversion to UP_2O_7, *Ultrason. Sonochem.*, 2015, **26**, 157–162.

105 D. Espino, Y. Haruvy-Manor, Y. Bar and Y. Mastai, Radical degradation processes initiated by catalytic nanoparticles of $CoFe_2O_4$ towards polymer waste application, *J. Polym. Environ.*, 2018, **26**, 3389–3396.

106 M. H. Khorasanizadeh, M. Ghiyasiyan-Arani, R. Monsef, M. Salavati-Niasari and H. Moayedi, Ultrasound-accelerated synthesis of uniform $DyVO_4$ nanoparticles as high activity visible-light-driven photocatalyst, *Ultrason. Sonochem.*, 2019, **59**, 104719.

107 S. R. Yousefi, O. Amiri and M. Salavati-Niasari, Control sonochemical parameter to prepare pure $Zn_{0.35}Fe_{2.65}O_4$ nanostructures and study their photocatalytic activity, *Ultrason. Sonochem.*, 2019, **58**, 104619.

108 A. Moghtada and R. Ashiri, Superiority of sonochemical processing method for the synthesis of barium titanate nanocrystals in contrast to the mechanochemical approach, *Ultrason. Sonochem.*, 2018, **41**, 127–133.

109 P. K. Vabbina, A. Kaushik, N. Pokhrel, S. Bhansali and N. Pala, Electrochemical cortisol immunosensors based on sonochemically synthesized zinc oxide 1D nanorods and 2D nanoflakes, *Biosens. Bioelectron.*, 2015, **63**, 124–130.

110 J. Zhu, S. Xu, H. Wang, J. Zhu and H. Chen, Sonochemical synthesis of CdSe hollow spherical assemblies via an in-situ template route, *Adv. Mater.*, 2003, **15**, 156–159.

111 Y. Zhang, L. Wang, D. Chu, H. Sun, A. Wang, Z. Ma, L. Yang, Y. Zhuang and Y. Bai, Fabrication of coupled twin-shaped hollow hemispherical calcium molybdate via a facile ultrasound-assisted approach, *CrystEngComm*, 2015, **17**, 2444–2449.

112 N. A. Dhas and K. S. Suslick, Sonochemical preparation of hollow nanospheres and hollow nanocrystals, *J. Am. Chem. Soc.*, 2005, **127**, 2368–2369.

113 J. H. Bang and K. S. Suslick, Sonochemical synthesis of nanosized hollow hematite, *J. Am. Chem. Soc.*, 2007, **129**, 2242–2243.

114 N. Du, H. Zhang, B. D. Chen, J. B. Wu, X. Y. Ma, Z. H. Liu, Y. Q. Zhang, D. R. Yang, X. H. Huang and J. P. Tu, Porous Co_3O_4 nanotubes derived from $Co_4(CO)_{12}$ clusters on carbon nanotube templates: a highly efficient material for Li-Battery applications, *Adv. Mater.*, 2007, **19**, 4505–4509.

115 J. Geng, J. Zhu, D. Lu and H. Chen, Hollow $PbWO_4$ nanospindles via a facile sonochemical route, *Inorg. Chem.*, 2006, **45**, 8403–8407.

116 R. L. Palomino, A. M. B. Miró, F. N. Tenorio, F. S. D. Jesús, C. A. C. Escobedo and S. Ammar, Sonochemical assisted

synthesis of $SrFe_{12}O_{19}$ nanoparticles, *Ultrason. Sonochem.*, 2016, **29**, 470–475.

117 R. L. P. Resendiz, F. S. D. Jesús, C. A. C. Escobedo, L. E. H. Cruz and A. M. B. Miró, Effect of sonication output power on the crystal structure and magnetism of $SrFe_{12}O_{19}$ nanoparticles, *Crystals*, 2018, **8**, 45.

118 E. L. S. Souza, J. C. Sczancoski, I. C. Nogueira, M. A. P. Almeida, M. O. Orlandi, M. S. Li, R. A. S. Luz, M. G. R. Filho, E. Longo and L. S. Cavalcante, Structural evolution, growth mechanism and photoluminescence properties of $CuWO_4$ nanocrystals, *Ultrason. Sonochem.*, 2017, **38**, 256–270.

119 J. Yu, J. Yu, W. Ho and L. Zhang, Preparation of highly photocatalytic active nano-sized TiO_2 particles via ultrasound irradiation, *Chem. Commun.*, 2001, **19**, 1942–1943.

120 S. A. Mansour, Non-isothermal crystallization kinetics of nano-sized amorphous TiO_2 prepared by facile sonochemical hydrolysis route, *Ceram. Int.*, 2019, **45**, 2893–2898.

121 M. V. Swapna and K. R. Haridas, An easier method of preparation of mesoporous anatase TiO_2 nanoparticles via ultrasonic irradiation, *J. Exp. Nanosci.*, 2016, **11**, 540–549.

122 Y. Peng, J. Ji, X. Zhao, H. Wan and D. Chen, Preparation of ZnO nanopowder by a novel ultrasound assisted non-hydrolytic sol-gel process and its application in photocatalytic degradation of C.I. Acid Red 249, *Powder Technol.*, 2013, **233**, 325–330.

123 P. J. Jodłowski, D. K. Chlebda, R. J. Jedrzejczyk, A. Dziedzicka, Ł. Kuterasinski and M. Sitarz, Characterisation of well-adhered ZrO_2 layers produced on structured reactors using the sonochemical sol-gel method, *Appl. Surf. Sci.*, 2018, **427**, 563–574.

124 J. J. Hinman and K. S. Suslick, Nanostructured materials synthesis using ultrasound, *Top. Curr. Chem.*, 2017, **375**, 12.

125 J. N. Coleman, M. Lotya, A. O'Neill, S. D. Bergin, P. J. King, U. Khan, K. Young, A. Gaucher, S. De, R. J. Smith, I. V. Shvets, S. K. Arora, G. Stanton, H. Y. Kim, K. Lee, G. T. Kim, G. S. Duesberg, T. Hallam, J. J. Boland, J. J. Wang, J. F. Donegan, J. C. Grunlan, G. Moriarty, A. Shmeliov, R. J. Nicholls, J. M. Perkins, E. M. Grieveson, K. Theuwissen, D. W. McComb, P. D. Nellist and V. Nicolosi, Two-dimensional nanosheets produced by liquid exfoliation of layered materials, *Science*, 2011, **331**, 568–571.

126 Y. Zhang, L. A. Huff, A. A. Gewirth and K. S. Suslick, Synthesis of manganese oxide microspheres by ultrasonic spray pyrolysis and their application as supercapacitors, *Part. Part. Syst. Charact.*, 2015, **32**, 899–906.

127 A. K. P. Mann, S. Wicker and S. E. Skrabalak, Aerosol-assisted molten salt synthesis of $NaInS_2$ nanoplates for use as a new photoanode material, *Adv. Mater.*, 2012, **24**, 6186–6191.

128 J. Fu, N. N. Daanen, E. E. Rugen, D. P. Chen and S. E. Skrabalak, Simple reactor for ultrasonic spray synthesis of nanostructured materials, *Chem. Mater.*, 2017, **29**, 62–68.

129 D. P. Chen, W. Bowers and S. E. Skrabalak, Aerosol-assisted combustion synthesis of single-crystalline $NaSbO_3$ nanoplates: a topotactic template for ilmenite $AgSbO_3$, *Chem. Mater.*, 2015, **27**, 174–180.

130 S. Sagadevan, I. Das, K. Pal, P. Murugasen and P. Singh, Optical and electrical smart response of chemically stabilized graphene oxide, *J. Mater. Sci.: Mater. Electron.*, 2017, **28**, 5235–5243.

131 T. Soltani and B. Lee, A benign ultrasonic route to reduced graphene oxide from pristine graphite, *J. Colloid Interface Sci.*, 2017, **486**, 337–343.

132 A. Ciesielski and P. Samori, Graphene via sonication assisted liquid-phase exfoliation, *Chem. Soc. Rev.*, 2014, **43**, 381–398.

133 Y. Hernandez, V. Nicolosi, M. Lotya, F. M. Blighe, Z. Sun, S. De, I. T. McGovern, B. Holland, M. Byrne, Y. K. Gun'Ko, J. J. Boland, P. Niraj, G. Duesberg, S. Krishnamurthy, R. Goodhue, J. Hutchison, V. Scardaci, V. A. C. Ferrari and J. N. Coleman, High-yield production of graphene by liquid-phase exfoliation of graphite, *Nat. Nanotechnol.*, 2008, **3**, 563–568.

134 J. Amaro-Gahete, A. Benítez, R. Otero, D. Esquivel, C. Jiménez-Sanchidrián, J. Morales, Á. Caballero and F. J. Romero-Salguero, A comparative study of particle size distribution of graphene nanosheets synthesized by an ultrasound-assisted method, *Nanomaterials*, 2019, **9**, 152.

135 E. A. Trusova, K. V. Kotsareva, A. N. Kirichenko, S. S. Abramchuk and I. A. Perezhogin, Sonochemical preparation and subsequent fixation of oxygen-free graphene sheets at *N*,*N*-dimethyloctylamine-aqua boundary, *Adv. Mater. Sci. Eng.*, 2018, 1–11.

136 A. H. Abdullah, Z. Ismail, A. S. Z. Abidin and K. Yusoh, Green sonochemical synthesis of few-layer graphene in instant coffee, *Mater. Chem. Phys.*, 2019, **222**, 11–19.

137 H. Ha and S. Jeong, Facile route to multi-walled carbon nanotubes under ambient conditions, *Korean J. Chem. Eng.*, 2016, **33**, 401–404.

138 V. B. Kumar, Z. Porat and A. Gedanken, Facile one-step sonochemical synthesis of ultrafine and stable fluorescent C-dots, *Ultrason. Sonochem.*, 2016, **28**, 367–375.

139 H. Li, X. He, Y. Liu, H. Huang, S. Lian, S. T. Lee and Z. Kang, One-step ultrasonic synthesis of water-soluble carbon nanoparticles with excellent photoluminescent properties, *Carbon*, 2011, **49**, 605–609.

140 K. Wei, J. Li, Z. Ge, Y. You and H. Xu, Sonochemical synthesis of highly photoluminescent carbon nanodots, *RSC Adv.*, 2014, **4**, 52230–52234.

141 R. Kumar, V. B. Kumar and A. Gedanken, Sonochemical synthesis of carbon dots, mechanism, effect of parameters, and catalytic, energy, biomedical and tissue engineering applications, *Ultrason. Sonochem.*, 2020, **64**, 105009.

142 M. Lu and L. Zhou, One-step sonochemical synthesis of versatile nitrogen-doped carbon quantum dots for

sensitive detection of Fe^{2+} ions and temperature in vitro, *Mater. Sci. Eng., C*, 2019, **101**, 352–359.

143 B. T. Mayers, K. Liu, D. Sunderland and Y. N. Xia, Sonochemical synthesis of trigonal selenium nanowires, *Chem. Mater.*, 2003, **15**, 3852–3858.

144 X. Li, Y. Li, S. Li, W. Zhou, H. Chu, W. Chen, I. L. Li and Z. Tang, Single crystalline trigonal selenium nanotubes and nanowires synthesized by sonochemical process, *Cryst. Growth Des.*, 2005, **5**, 911–916.

145 M. Panahi-Kalamuei, M. Salavati-Niasari, Z. Zarghami, M. Mousavi-Kamazani, H. Taqriri and A. Mohsenikia, Synthesis and characterization of Se nanostructures via co-precipitation, hydrothermal, microwave and sonochemical routes using novel starting reagents for solar cells, *J. Mater. Sci.: Mater. Electron.*, 2015, **26**, 2851–2860.

146 A. P. C. Bedini, B. Klingebiel, M. Luysberg and R. Carius, Sonochemical synthesis of hydrogenated amorphous silicon nanoparticles from liquid trisilane at ambient temperature and pressure, *Ultrason. Sonochem.*, 2017, **39**, 883–888.

147 H. Kim, C. Lee and B. Kim, Sonochemical synthesis of silica particles and their size control, *Appl. Surf. Sci.*, 2015, **380**, 305–308.

148 M. Masjedi-Arani, D. Ghanbari, M. Salavati-Niasari and S. Bagheri, Sonochemical synthesis of spherical silica nanoparticles and polymeric nanocomposites, *J. Cluster Sci.*, 2016, **27**, 39–53.

149 S. Sankar, N. Kaur, S. Lee and D. Y. Kim, Rapid sonochemical synthesis of spherical silica nanoparticles derived from brown rice husk, *Ceram. Int.*, 2018, **44**, 8720–8724.

150 S. Jiang, G. Tang, Z. Bai and Y. Pan, Ultrasonic-assisted synthesis of hollow mesoporous silica as a toxic gases suppressant, *Mater. Lett.*, 2019, **247**, 139–142.

151 D. Chen, S. H. Yoo, Q. Huang, G. Ali and S. O. Cho, Sonochemical synthesis of Ag/AgCl nanocubes and their efficient visible-light-driven photocatalytic performance, *Chem.–Eur. J.*, 2012, **18**, 5192–5200.

152 S. Mao, R. Bao, D. Fang and J. Yi, Facile synthesis of Ag/AgX (X = Cl, Br) with enhanced visible-light-induced photocatalytic activity by ultrasonic spray pyrolysis method, *Adv. Powder Technol.*, 2018, **29**, 2670–2677.

153 M. Abbas, W. Tawfik and J. Chen, CdO nanorods and $Cd(OH)_2$/Ag core/satellite nanorods: rapid and efficient sonochemical synthesis, characterization and their magnetic properties, *Ultrason. Sonochem.*, 2018, **40**, 577–582.

154 M. Abbas, Y. Xue, J. Zhang and J. Chen, Ultrasound induced morphology-controlled synthesis of Au nanoparticles decorated on Fe_2O_3/ZrO_2 catalyst and their catalytic performance in Fischer-Tropsch synthesis, *Fuel Process. Technol.*, 2019, **187**, 63–72.

155 V. Belova, T. Borodina, H. Moehwald and D. G. Shchukin, The effect of high intensity ultrasound on the loading of Au nanoparticles into titanium dioxide, *Ultrason. Sonochem.*, 2011, **18**, 310–317.

156 H. M. Xiong, D. G. Shchukin, H. Moehwald, Y. Xu and Y. Y. Xia, Sonochemical synthesis of highly luminescent zinc oxide nanoparticles doped with magnesium(II), *Angew. Chem., Int. Ed.*, 2009, **48**, 2727–2731.

157 Y. Li, R. Lei and S. Xu, Combination of ionic liquid and sonication: a fast, mild and green way to fabricate Europium-doped lanthanide nanophosphates, *ChemistrySelect*, 2016, **1**, 4861–4867.

158 K. N. Venkatachalaiaha, H. Nagabhushana, G. P. Darshan, R. B. Basavaraj, B. Daruka Prasad and S. C. Sharma, Structural, morphological and photometric properties of sonochemically synthesized Eu^{3+} doped Y_2O_3 nanophosphor for optoelectronic devices, *Mater. Res. Bull.*, 2017, **94**, 442–455.

159 H. Terraschke, J. Olchowka, E. Geringer, A. V. Rodrigues and C. Wickleder, Facile ionic liquid-assisted strategy for direct precipitation of Eu^{2+}-activated nanophosphors under ambient conditions, *Small*, 2018, **14**, 1703707.

160 M. K. Akbari, Z. Hai, Z. Wei, R. K. Ramachandran, C. Detavernier, M. Patel, J. Kim, F. Verpoort, H. Lu and S. Zhuiykov, Sonochemical functionalization of the lowdimensional surface oxide of Galinstan for heterostructured optoelectronic applications, *J. Mater. Chem. C*, 2019, **7**, 5584–5595.

161 V. B. Kumar, I. Perelshtein, A. Lipovsky, Z. Porat and A. Gedanken, The sonochemical synthesis of Ga@C-dots particles, *RSC Adv.*, 2015, **5**, 25533–25540.

162 V. B. Kumar, M. Monte, O. Mathon, S. Pascarelli, Z. Porat and A. Gedanken, The interaction between molten gallium and the hydrocarbon medium induced by ultrasonic energy—can gallium carbide be formed, *J. Am. Ceram. Soc.*, 2017, **100**, 3305–3315.

163 I. Nissan, V. B. Kumar, Z. Porat, D. Makovec, O. Shefi and A. Gedanken, Sonochemically-fabricated Ga@C-dots@Ga nanoparticle-aided neural growth, *J. Mater. Chem. B*, 2017, **5**, 1371–1379.

164 J. Walter, M. Nishioka and S. Hara, Ultrathin platinum nanoparticles encapsulated in a graphite lattices prepared by a sonochemical approach, *Chem. Mater.*, 2001, **13**, 1828–1833.

165 J. E. Jones, M. C. Cheshire, D. J. Casadonte and J. C. C. Phifer, Facile sonochemical synthesis of graphite intercalation compounds, *Org. Lett.*, 2004, **6**, 1915–1917.

166 Z. Cheng, Y. Kong, L. Fan and Z. Liu, Ultrasound-assisted Li^+/Na^+ co-intercalated exfoliation of graphite into few-layer graphene, *Ultrason. Sonochem.*, 2020, **66**, 105108.

167 A. F. S. Salazar, T. Chave, A. Ayral, S. I. Nikitenko, V. Hulea, P. J. Kooyman, F. D. Tichelaar, S. Perathoner and P. Lacroix-Desmazes, Engineering of silica-supported platinum catalysts with hierarchical porosity combining latex synthesis, sonochemistry and sol-gel process—I. material preparation, *Microporous Mesoporous Mater.*, 2016, **234**, 207–214.

168 J. Zhang, B. Zhang and X. Zhang, Enhanced catalytic activity of ternary NiCoPd nanocatalyst dispersed on carbon nanotubes toward methanol oxidation reaction in

alkaline media, *J. Solid State Electrochem.*, 2017, **21**, 447–453.

169 C. Okoli, K. A. Kuttiyiel, K. Sasaki, D. Su, D. Kuila, D. Mahajan and R. R. Adzic, Highly dispersed carbon supported PdNiMo core with Pt monolayer shell electrocatalysts for oxygen reduction reaction, *J. Electrochem. Soc.*, 2018, **165**, J3295–J3300.

170 Y. Zhou, J. Yang, C. Zhu, D. Du, X. Cheng, C. H. Yen, C. M. Wai and Y. Lin, Newly designed graphene cellular monolith functionalized with hollow Pt-M (M = Ni, Co) nanoparticles as the electrocatalyst for oxygen reduction reaction, *ACS Appl. Mater. Interfaces*, 2016, **8**, 25863–25874.

171 M. Abbas, Z. Chen and J. Chen, Shape- and size-controlled synthesis of Cu nanoparticles wrapped on RGO nanosheet catalyst and their outstanding stability and catalytic performance in the hydrogenation reaction of dimethyl oxalate, *J. Mater. Chem. A*, 2018, **6**, 19133–19142.

172 A. I. Argüelles-Pesqueira, N. M. Diéguez-Armenta, A. K. Bobadilla-Valencia, S. K. Nataraj, A. Rosas-Durazo, R. Esquivel, M. E. Alvarez-Ramos, R. Escudero, P. Guerrero-German, J. A. Lucero-Acuña and P. Zavala-Rivera, Low intensity sonosynthesis of iron carbide@iron oxide core-shell nanoparticles, *Ultrason. Sonochem.*, 2018, **49**, 303–309.

173 F. Xu, Y. Yuan, H. Han, D. Wu, Z. Gao and K. Jiang, Synthesis of ZnO/CdS hierarchical heterostructure with enhanced photocatalytic efficiency under nature sunlight, *CrystEngComm*, 2012, **14**, 3615–3622.

174 S. D. Balgude, Y. A. Sethi, B. B. Kale, D. P. Amalnerkar and P. V. Adhyapak, ZnO decorated Sn_3O_4 nanosheet nanoheterostructure: a stable photocatalyst for water splitting and dye degradation under natural sunlight, *RSC Adv.*, 2019, **9**, 10289–10296.

175 M. Mousavi-Kamazani and S. Ashrafi, Single-step sonochemical synthesis of Cu_2O-CeO_2 nanocomposites with enhanced photocatalytic oxidative desulfurization, *Ultrason. Sonochem.*, 2020, **63**, 104948.

176 M. D. Purkayastha, S. Denrah, N. Singh, M. Sarkar, G. K. Darbha and T. P. Majumder, Crystal structure dependent photocatalytic degradation of manganese and titanium oxides composites, *SN Appl. Sci.*, 2020, **2**, 1126.

177 S. Alizadeh, N. Fallah and M. Nikazar, An ultrasonic method for the synthesis, control and optimization of CdS/TiO_2 core-shell nanocomposites, *RSC Adv.*, 2019, **9**, 4314–4324.

178 M. Zhang, Q. Shang, Y. Wan, Q. Cheng, G. Liao and Z. Pan, Self-template synthesis of double-shell TiO_2@ZIF-8 hollow nanospheres via sonocrystallization with enhanced photocatalytic activities in hydrogen generation, *Appl. Catal., B*, 2019, **241**, 149–158.

179 C. Cau and S. I. Nikitenko, Mechanism of $W(CO)_6$ sonolysis in diphenylmethane, *Ultrason. Sonochem.*, 2012, **19**, 498–502.

180 R. Miyatani, Y. Kobayashi and Y. Yamada, Thermal reaction of sonochemically prepared amorphous Fe/C, *Hyperfine Interact.*, 2017, **238**, 61.

181 B. Li, S. Chen, J. Tian, M. Gong, H. Xu and L. Song, Amorphous nickel-iron oxides/carbon nanohybrids for an efficient and durable oxygen evolution reaction, *Nano Res.*, 2017, **10**, 3629–3637.

182 J. Guo, S. Zhu, Z. Chen, Y. Li, Z. Yu, Q. Liu, J. Li, C. Feng and D. Zhang, Sonochemical synthesis of TiO_2 nanoparticles on graphene for use as photocatalyst, *Ultrason. Sonochem.*, 2011, **18**, 1082–1090.

183 G. Karkera, S. G. Chandrappa and A. S. Prakash, Viable synthesis of porous $MnCo_2O_4$/graphene composite by sonochemical grafting: a high-rate-capable oxygen cathode for Li-O_2 batteries, *Chem.–Eur. J.*, 2018, **24**, 17303–17310.

184 X. Han, R. Li, S. Qiu, X. Zhang, Q. Zhang and Y. Yang, Sonochemistry-enabled uniform coupling of SnO_2 nanocrystals with graphene sheets as anode materials for lithium-ion batteries, *RSC Adv.*, 2019, **9**, 5942–5947.

185 Q. Wang, P. Chen, X. Zeng, H. Jiang, F. Meng, X. Lia, T. Wang, G. Zeng, L. Liu, H. Shu and X. Luo, Synthesis of (ZrO_2-Al_2O_3)/GO nanocomposite by sonochemical method and the mechanism analysis of its high defluoridation, *J. Hazard. Mater.*, 2020, **381**, 120954.

186 C. Cobianu, N. Dumbravescu, B. Serban, O. Buiu, F. Comanescu, C. Romanitan, M. Danila, V. Avramescu and O. Ionescu, *Facile 3D nanostructured ZnO-graphene hybrids for gas sensing applications, International semiconductor conference*, 2019, p. 19222671.

187 M. Khairy, E. M. Naguib and M. M. Mohamed, Enhancement of photocatalytic and sonophotocatalytic degradation of 4-nitrophenol by ZnO/graphene oxide and ZnO/carbon nanotube nanocomposites, *J. Photochem. Photobiol., A*, 2020, **396**, 112507.

188 D. Ravelo-Acuña, J. A. Fuentes-García, H. T. Yee-Madeira, A. I. Diaz-Cano, G. F. Goya and J. Santoyo-Salazar, Sonochemical magnetite encapsulation in silica at low irradiation power, *Mater. Lett.*, 2019, **250**, 103–107.

189 G. L. Sharipov, A. M. Abdrakhmanov, B. M. Gareev and A. A. Tukhbatullin, Porous SiO_2 nanoparticles containing ruthenium or sulfur compounds: sonochemical producing and sonoluminescence in aqueous suspensions, *Ultrason. Sonochem.*, 2020, **61**, 104842.

190 S. Seok, M. A. Hussain, K. J. Park, J. W. Kim and D. H. Kim, Sonochemical synthesis of PdO@silica as a nanocatalyst for selective aerobic alcohol oxidation, *Ultrason. Sonochem.*, 2016, **28**, 178–184.

191 S. Zinatloo-Ajabshir, S. Mortazavi-Derazkola and M. Salavati-Niasari, Nd_2O_3-SiO_2 nanocomposites: a simple sonochemical preparation, characterization and photocatalytic activity, *Ultrason. Sonochem.*, 2018, **42**, 171–182.

192 M. S. Elshikh, F. M. A. Al-Hemaid, T. Chen, S. Chinnapaiyan, M. A. Ali and S. Chen, Sonochemical synthesis of graphitic carbon nitrides-wrapped bimetal oxide nanoparticles hybrid materials and their electrocatalytic activity for xanthine electro-oxidation, *Ultrason. Sonochem.*, 2020, **64**, 105006.

193 S. Mahzoon, M. Haghighi and S. M. Nowee, Sonoprecipitation fabrication of enhanced electron transfer $Cu(OH)_2/g\text{-}C_3N_4$ nanophotocatalyst with promoted H_2-Production activity under visible light irradiation, *Renewable Energy*, 2020, **150**, 91–100.

194 B. Wang, X. Li, H. Wu, G. Xu, X. Zhang, X. Shu, J. Lv and Y. Wu, Synthesis of Ni-$MoS_x/g\text{-}C_3N_4$ for photocatalytic hydrogen evolution under visible light, *Chemcatchem*, 2020, **12**, 911–916.

195 A. Gopalarishnan and S. Badhulika, Facile sonochemical assisted synthesis of hybrid red-black phosphorus/sulfonated porous carbon composite for highperformance supercapacitors, *Chem. Commun.*, 2020, **56**, 7096–7099.

196 H. Teymourinia, M. H. Darvishnejad, O. Amiri, M. Salavati-Niasari, A. Reisi-Vanani, E. Ghanbari and H. Moayedi, GQDs/Sb_2S_3/TiO_2 as a co-sensitized in DSSs: improve the power conversion efficiency of DSSs through increasing light harvesting by using as-synthesized nanocomposite and mirror, *Appl. Surf. Sci.*, 2020, **512**, 145638.

197 Y. Orooji, S. Mortazavi-Derazkola, S. M. Ghoreishi, M. Amiri and M. Salavati-Niasari, Mesopourous $Fe_3O_4@SiO_2$-hydroxyapatite nanocomposite: green sonochemical synthesis using strawberry fruit extract as a capping agent, characterization and their application in sulfasalazine delivery and cytotoxicity, *J. Hazard. Mater.*, 2020, **400**, 123140.

198 M. A. Ebrahimzadeh, S. Mortazavi-Derazkola and M. A. Zazouli, Eco-friendly green synthesis of novel magnetic $Fe_3O_4/SiO_2/ZnO\text{-}Pr_6O_{11}$ nanocomposites for photocatalytic degradation of organic pollutant, *J. Rare Earths*, 2020, **38**, 13–20.

199 X. Tang, E. Kröger, A. Nielsen, S. Schneider, C. Strelow, A. Mews and T. Kipp, Fluorescent metal-semiconductor hybrid structures by ultrasound-assisted in situ growth of gold nanoparticles on silica-coated CdSe-dot/CdS-rod nanocrystals, *Chem. Mater.*, 2019, **31**, 224–232.

200 C. Wang, J. Wang, P. Li, Z. Rong, X. Jia, Q. Ma, R. Xiao and S. Wang, Sonochemical synthesis of highly branched flower-like $Fe_3O_4@SiO_2@Ag$ microcomposites and their application as versatile SERS substrates, *Nanoscale*, 2016, **8**, 19816–19828.

201 S. Mohammadi-Aghdam, Sonochemical method for the preparation of magnetic nanoparticles employing green precursors and its composite with praseodymium(III) nanoparticles for photocatalytic degradation of rhodamine B, *J. Mater. Sci.: Mater. Electron.*, 2018, **29**, 5702–5709.

202 T. P. Shende, B. A. Bhanvase, A. P. Rathod, D. V. Pinjari and S. H. Sonawane, Sonochemical synthesis of Graphene-Ce-TiO_2 and Graphene-Fe-TiO_2 ternary hybrid photocatalyst nanocomposite and its application in degradation of crystal violet dye, *Ultrason. Sonochem.*, 2018, **41**, 582–589.

203 D. Muniswamy, H. Nagabhushana, R. B. Basavaraj, G. P. Darshan and D. Prasad B, Surfactant-assisted $BaTiO_3:Eu^{3+}@SiO_2$ core-shell superstructures obtained by ultrasonication method: dormant fingerprint visualization and red component of white light-emitting diode applications, *ACS Sustainable Chem. Eng.*, 2018, **6**, 5214–5226.

204 A. Sandhyarani, R. B. Basavaraj, G. P. Darshan, H. Nagabhushana and M. K. Kokila, Influence of surface modification on enhancement of luminescent properties of $SiO_2@SrTiO_3:Dy^{3+}$ nanopowders: probe for visualization of sweat pores present in latent fingerprints, *Optik*, 2019, **181**, 1139–1157.

205 Z. Li, T. Zhuang, J. Dong, L. Wang, J. Xia, H. Wang, X. Cui and Z. Wang, Sonochemical fabrication of inorganic nanoparticles for applications in catalysis, *Ultrason. Sonochem.*, 2021.